

# An atomistic insight to moiré reconstruction in Twisted Bilayer Graphene beyond magic angle

Aditya Dey\*,<sup>1, a)</sup> Shoieb Ahmed Chowdhury,<sup>1, a)</sup> Tara Peña,<sup>2</sup> Sobhit Singh,<sup>1</sup> Stephen M. Wu,<sup>2, b)</sup> and Hesam Askari<sup>1</sup>

<sup>1)</sup> *Department of Mechanical Engineering, University of Rochester, New York*

<sup>2)</sup> *Department of Electrical and Computer Engineering, University of Rochester, Rochester, New York*

(\*Electronic mail: adey2@ur.rochester.edu)

Twisted bilayer graphene exhibits electronic properties that are highly correlated with the size and arrangement of moiré patterns. While rigid rotation of two layers creates the topology of moiré patterns, local rearrangements of the atoms due to interlayer van der Waals interactions result in atomic reconstruction within the moiré cells. The ability to manipulate these patterns by controlling twist angle and/or externally applied strain provides a promising route to tune their properties. While this phenomenon has been extensively studied for angles close to or smaller than the magic angle ( $\theta_m=1.1^\circ$ ), its extent for higher angles and how it evolves with strain is unknown and is believed to be mostly absent at high angles. We use theoretical and numerical analyses to resolve reconstruction in angles above  $\theta_m$  using interpretive and fundamental physical measures. In addition, we propose a method to identify local regions within moiré cells and track their evolution with strain for a range of representative high twist angles. Our results show that reconstruction is actively present beyond the magic angle and its contribution to the evolution of the moiré cells is major. Our theoretical method to correlate local and global phonon behavior provides further validation on the role of reconstruction at higher angles. Our findings provide a better understanding of moiré reconstruction in large twist angles and the evolution of moiré cells in the presence of strain, that might be very crucial for twistrionics-based applications.

## I. Introduction

Engineering two-dimensional (2D) materials by controlling the stacking orientation of atomic layers have emerged as a powerful technique to manipulate their mechanical and opto-electronic properties. Bilayer graphene (BLG) is one of the simplest van der Waals (vdW) structures that display diverse physical properties such as contrasting electronic structures depending on the stacking arrangement<sup>1-4</sup>. Introducing a relative rotation between the layers forms the Twisted Bilayer Graphene (TBG) in which the atoms create a periodic hexagonal superlattice called ‘moiré pattern’ (MP)<sup>5-7</sup>. Emergence of this pattern is due to the atoms occupying different relative interlayer positions compared to BLG with a global size that is inversely correlated with the twist angle ( $\theta$ ) as  $L_m = a/(2 \sin(\theta/2))$  where  $a$  is the lattice constant of graphene. Application of other mechanical stimuli such as inequivalent strain to the individual layers of TBG can further manipulate the shape of the pattern. Thus, the combination of hetero-straining process and twist provides a promising outlook for creating unique shapes and geometries of MPs for exciting opto-electronic applications<sup>8-10</sup>.

The atomic arrangements within MPs are influenced by the interlayer vdW forces between the atoms that considerably influence the atomic arrangement landscape. To manifest this influence, we can consider a hypothetical intermediate configuration where atoms are rigidly twisted in their plane and consequently, the well-defined BLG stacking configurations of AA, AB and SP types with their spatial variations will emerge<sup>11,12</sup>. Upon allowing atomic reconfiguration, an

atomic-scale reconstruction occurs and local stacked regions evolve to their true minimum local energy configuration. This process is known as moiré reconstruction<sup>13,14</sup>. Previous studies have reported this phenomenon for low angle TBGs, especially in the vicinity of or below the ‘magic angle’ ( $\theta_m = 1.1^\circ$ )<sup>15,16</sup>. As the size of MP shrinks with an increase in  $\theta$  and leaves less space for reconfiguration of atoms, experimental observation of moiré reconstruction becomes a challenge and is generally assumed to be absent for  $\theta > 2^\circ$ <sup>15,17,18</sup>. Since the large angle TBGs contain the same atomic registry but only over a smaller region compared to the small twist angles, it is unreasonable to expect moiré reconstruction should suddenly become absent. The interplay between the in-plane elastic energy and interlayer vdW energy is still expected to contribute to reconstruction at higher angles due to the same fundamental physics. Nevertheless, its extent remains unknown due to the current limitations of experimental methods.

Recent experimental studies have demonstrated the ability to control TBGs with and without strain and characterize moiré reconstruction for smaller  $\theta$  systems<sup>8,14,19-23</sup>. Imaging techniques such as STM and TEM become challenging when feature size becomes comparable to their resolution. As the size of MP decreases with increasing twist, imaging for  $\theta > 2^\circ$  systems become unfeasible<sup>11,24</sup>. Therefore, the current understanding of reconstruction through experimental visualization is limited to low angle twists and largely based on image analysis techniques rather than physical measurable quantities. Optical procedures such as Raman spectroscopy offer an expedient method to characterize TBGs irrespective of their size and twist angle<sup>25-28</sup> but such methods predominantly extract the collective behavior of TBGs spanning numerous MPs. Therefore the global vibrational behavior obtained by Raman cannot be readily used to infer stacking and the extent of reconstruction without an interrelation of phonon

<sup>a)</sup>These authors contributed equally to this work

<sup>b)</sup>Department of Physics and Astronomy, University of Rochester, Rochester, New York

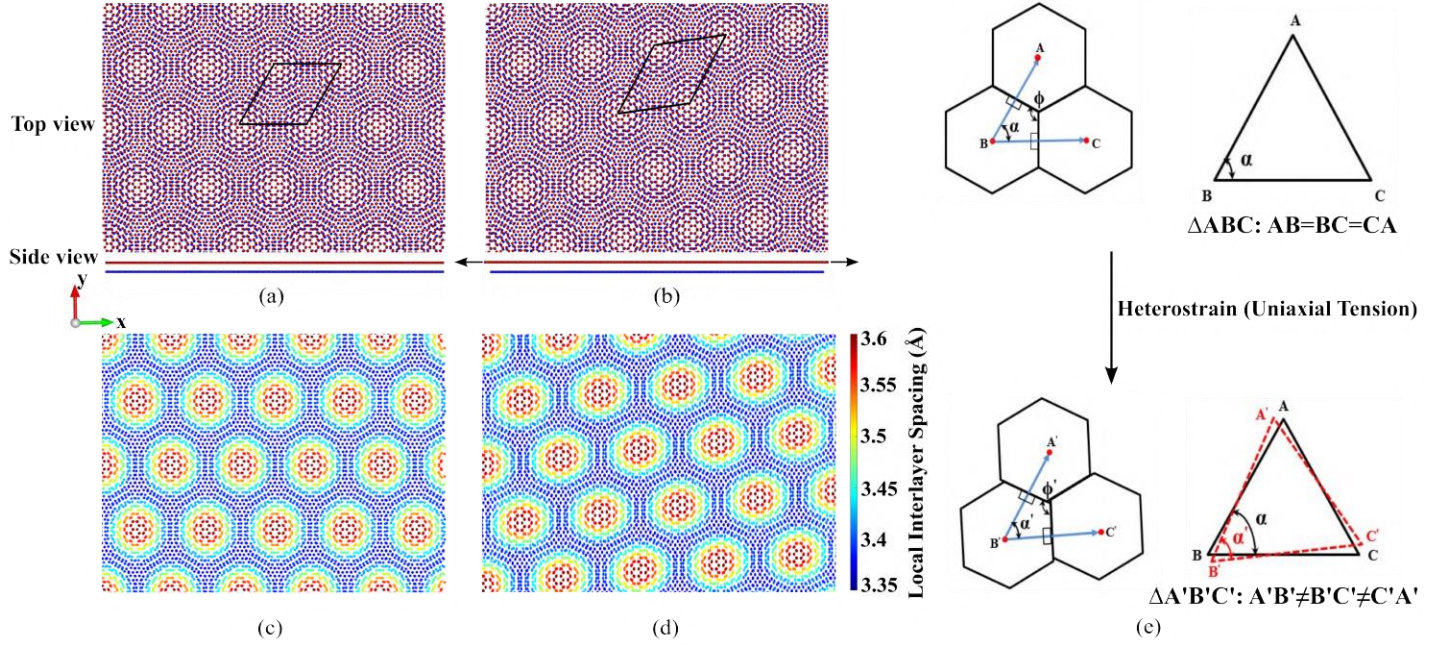


FIG. 1: **Atomistic model.** Relaxed atomistic structures illustrate how periodic moiré superlattice is formed and how its shape evolves with strain (a & b). Unlike BLG where a single interlayer distancing is expected, twist results in spatial variations of interlayer distancing with as shown for (c) unstrained and (d) strained TBGs. Data presented for the twist angle of  $\theta = 6^\circ$  and uniaxial strain of 1% . (e) Real space geometric analysis demonstrating the distortion of MPs with applied uniaxial tension to the top layer.

behavior between local sub-domains and the bulk of TBG. Atomistic analyses offer an alternative tool to study atomic arrangements locally with a fine resolution and allow for tracking of atomistic evolution with varying twist angle<sup>11,20,29–31</sup>. Current works are heavily concentrated on or below the magic angle and do not explain the correlation of local and global behavior of TBGs and moreover, have not studied the evolution of MPs with strain. As a result, there remains an outstanding question about the viability and the role of reconstruction at higher angles and how local and global vibrational properties are correlated.

In this work, we utilized a combination of first-principles and molecular statics atomistic simulations to examine the local domains in TBGs and how global vibrational behavior is tied to changes in local atomic registries. Based on physical parameters that include interlayer spacing and interlayer energy, our method associates each atom to known stacking types of the constituent bi-layer graphene and calculates their resultant area fraction and traces the evolution of local sub-domains, and demonstrates evidence of moiré reconstruction for larger  $\theta$  TBG systems. This paper presents an effective set of criteria for the identification of local stacking and reconstruction phenomena in TBGs that are valid with or without the application of strain. In addition, we demonstrate the correlation between local and global vibrational characteristics of TBGs and how it validates our results on reconstructed structures, especially at higher angles. The methods presented in this paper are devised for graphene but further adaptations are

possible for other 2D materials.

## II. Methods

### A. Atomistic modeling.

All the TBG structures are constructed by rotating the top layer of Bernal stacked bilayer graphene with respect to its bottom layer. The moiré lattice is created by identifying a common periodic lattice for the two layers. Using the TBG commensurability conditions, we have modeled their real and reciprocal space lattice parameters<sup>32,33</sup>. The  $\vec{q}$  vector or reciprocal lattice parameter of TBG moiré lattice is given as  $\vec{q} = \vec{b}' - \vec{b}$ , where  $\vec{b}$  and  $\vec{b}'$  denote the reciprocal lattice vectors of the bottom layer and rotated top layer respectively. When heterostrain is applied, the strained  $\vec{q}$  vector is expressed as  $\vec{q}_i^\varepsilon = \vec{b}^\varepsilon - \vec{b}$ , where  $\vec{b}^\varepsilon$  denotes the strained top layer. The mathematical expressions of  $\vec{b}^\varepsilon$  are deduced in Supplementary section II. All the atomistic models are relaxed using density functional theory (DFT) simulations, except for  $\theta = 1.08^\circ$  system. Because of a large moiré lattice for this structure (11164 atoms), DFT becomes forbiddingly inefficient and thus, we use force-field potentials for relaxing this structure.

### B. DFT calculations.

The real space lattices of TBG systems were constructed using ATOMISTIX TOOLKIT (QuantumATK) package<sup>34</sup>. All the first-principles simulations were conducted with generalized gradient approximation (GGA) assimilated in Quantum Espresso open source package<sup>35,36</sup>. The Perdew-Burke-

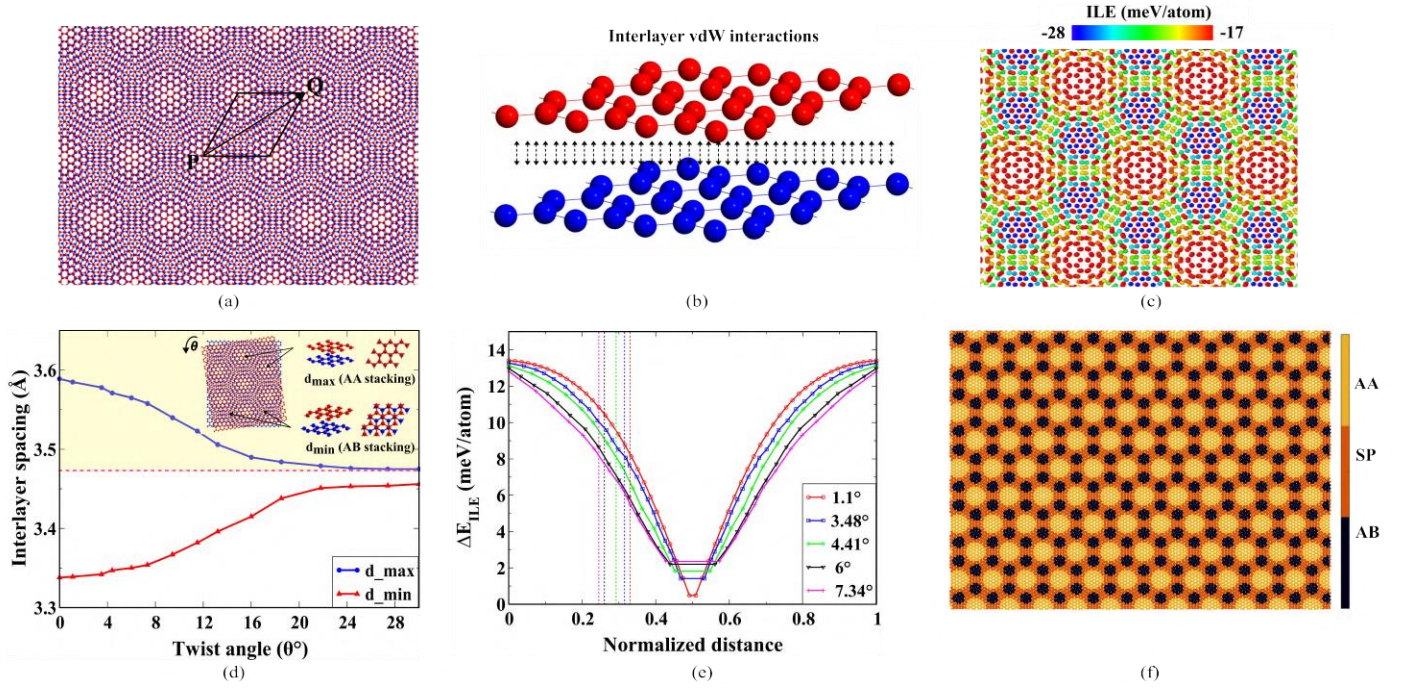


FIG. 2: **Local stacking identification method.** (a) Path PQ along the center of one moiré pattern to the other ( $\theta = 6^\circ$ ) (b) Illustration of interlayer energy (ILE) which is the energy contribution of vdW interactions. (c) ILE contour plot for unstrained  $\theta = 6^\circ$  system. (d) Variation of interlayer spacing (ILS) with respect to moiré twist angles; Horizontal dotted line (magenta) shows the minima of maximum ILS ( $d_{max}$ ) obtained throughout a span of low and high angles TBGs. (e) Variation of ILE difference for five representative  $\theta$  (the dotted line shows the energy difference at soliton width boundary) (f) Contour plot demonstrating individual stacking type locally, obtained after implementing classification method.

Ernzerhof (PBE) form along with GGA has been used as the exchange-correlation functional<sup>37</sup>. Ion-electron interactions for carbon atoms in TBGs have been described by ultrasoft pseudopotentials<sup>38</sup>. All technical details about DFT parameters are given in Supplementary information-Section I.

### C.MS simulations.

Molecular statics simulations were done using LAMMPS open source software<sup>39,40</sup>. The unstrained, DFT relaxed TBG moiré lattice was transformed into an orthogonal cell for performing MS simulations. The simulation box is considered with free surface boundary conditions allowing us to account for the aperiodic crystal geometry (or moiré lattice mismatch) due to strain applied to one of the layers. The uniaxial strain was incremented by  $\pm 0.1\%$  up to the final strain magnitude of  $\pm 1\%$ . The snapshots of the structure at different strain magnitudes were taken in Ovito open visualization tool. Further computational details are mentioned in Supplementary section I.

## III. Results and Discussions

### A. Global structural analysis of pristine and strained TBGs.

We have studied a number of TBG systems between  $\theta = 1.08^\circ$  and  $13.2^\circ$  to perform our analysis on MPs close to  $\theta_m$  as well as outside the limit of small angles. For simplicity, most of the presented data include three representative TBG systems  $\theta = 1.08^\circ$ ,  $6^\circ$  and  $13.2^\circ$ . The MP geometries

are modeled using the well-defined commensurability conditions of TBG systems and relaxed using first-principles or force field optimization techniques (see Methods) (Fig. 1(a)). Since the local domains in TBG evolve through high symmetry BLG stacking, we can observe topographical variation in the structure<sup>41,42</sup> represented by interlayer spacing (ILS) contour plot (Fig. 1(c)). The centers of hexagonal MPs have regions of atoms where AA stacking exists<sup>13,43</sup>. These central regions are surrounded by two domains, AB and BA stacking, which are energetically degenerate but topologically inequivalent. Since both of these stacking represent the Bernal graphene, they can be categorized as one<sup>44,45</sup>. The boundaries of these AB/BA regions are separated by segments referred as strain solitons. The shear strain which generates due to two inequivalent stacking domains facing each other is confined within those segments with characteristic width referred to as the soliton width<sup>43</sup>. The atomic structure in the soliton regions corresponds to SP stacking which is an intermediate configuration between AB (or BA) and AA. A TBG system displays an out-of-plane corrugation in its structure caused by local ILS variation with AA regions having the highest spacing followed by SP and AB regions<sup>11,12,30</sup>.

On employing heterostrain, we observed a similar topographical feature with distorted MPs due to the inequivalence of strain in each layer that resulted in an oblique moiré arrangement<sup>8</sup> (Fig. 1(b), (d) for tension and Fig. S1 for com-



pression). A geometric analysis is represented to explicate the angular change due to distortion and rigid rotation (Fig. 1(e)) by deducing the expressions of their reciprocal lattice ( $\vec{q}$ ) vectors (see Supplementary). The change in  $\vec{q}$  vector with uniaxial strain triggers the distortion in MPs<sup>27,46</sup>. As shown in Fig. 1(e), the boundaries of MPs resemble a hexagon. On connecting the centers of adjacent MPs, we can draw a triangle ( $\triangle ABC$ ) with  $\vec{A} \rightarrow \vec{B}$  and  $\vec{B} \rightarrow \vec{C}$  as the moiré lattice vectors and  $\alpha$  being the angle between them. In unstrained condition, the magnitude of vectors  $|\vec{A} \rightarrow \vec{B}| = |\vec{B} \rightarrow \vec{C}| = L_m$  ( $L_m$  = Length of MP) and the angles are  $\alpha = 60^\circ$ ,  $\varphi = 120^\circ$ . As the  $\vec{q}$  vector changes with uniaxial heterostrain,  $\triangle ABC$  transforms to  $\triangle A'B'C'$  such that  $|\vec{A}' \rightarrow \vec{B}'| \neq |\vec{B}' \rightarrow \vec{C}'|$ . The deformed moiré lattice can be quantified with a change in  $\alpha$  with the applied strain (Fig. S2). The expressions of moiré reciprocal lattice vectors, show the geometrical changes enforced upon hetero-straining these systems (Supplementary section II).

### B. Classification method to identify local domains.

The deformation of MP with strain gives rise to changes in their local sub-domains and it is important to examine them for quantifying their contribution to global physical behavior. Traversing along a diagonal of MP (path PQ in Fig. 2(a)), i.e., from the center of one moiré pattern to the center of its second nearest neighbor, we expect to cross all the locally stacked regions: AA, AB, SP, BA, and AA<sup>11,43,45</sup>. Since we aim to develop a criteria to classify each atom into one of these stacking, we first examined the atoms along the path PQ. To perform the stacking identification, we initially used the ILS parameter  $d$  because the local domains in TBGs vary in interlayer distancing. Since pristine BLG stacking follows an increasing ILS trend from AB to SP and finally the AA region,  $d_{max}$  (maximum ILS) and  $d_{min}$  (minimum ILS) in TBGs can be respectively understood as the ILS of AA and AB regions. By examining the range of ILS ( $d_{max}$  and  $d_{min}$ ) over different possible twist angles (Fig. 2(d)) we identify the minimum value of  $d_{max}$  (3.475Å) and classify atoms above this ILS threshold as AA. It should be noted that this does not misclassify AB and SP because this threshold is quite above the ILS of pristine AB (3.33Å) and SP (3.38Å). Due to the small ILS difference between AB and SP, the same ILS parameter cannot be used to identify the rest of the stackings.

We introduced another parameter called 'interlayer energy' (ILE) to distinguish between AB and SP according to their energy, rather than ILS. The ILE is a physical measure of vdW interaction between atoms in two different layers, as illustrated by the schematic in Fig. 2(b). It is obtained by computing the vdW part of the total potential energy between C-atoms in different layers Fig. 2(c). Since these local domains have indistinguishable and strong in-plane covalent bonds, their total potential energy is predominantly sourced from the in-plane interactions, which show little variance risen from their interlayer configuration. Moreover, with applied strain, the changes in total potential energy due to stretching and compressing of the in-plane bonds are orders of magnitude higher than their interlayer vdW counterparts. This motivates the use of vdW interaction energy and its variations for identification purposes. However, being a per-atom quantity there

are a lot of fluctuations in ILE magnitudes, most prominently observed in AB regions (2(c)). Moreover, if the average ILE magnitude is used with respect to their bonded neighbors, it will result in an insignificant difference between AB and SP sub-domains. Hence to account for this, we calculated the average ILE difference ( $\Delta E_{ILE}$ ) of each atom with its bonded neighbors. Although it can be difficult to separate AA and SP regions since they have minimal fluctuations in ILE, this parameter easily allows to classify AB stacked atoms as they have the highest variations in energy with neighbors. Based on the  $\Delta E_{ILE}$  analysis for five representative TBGs (Fig. 2e), we have identified the  $\Delta E_{ILE}$  threshold at the soliton boundary (SP width) and classified atoms above that threshold as AB. The infinitesimal difference in these thresholds allowed us to define a  $\theta$ -independent  $\Delta E_{ILE}$  value for identifying the two stackings (see Supplementary for details). It is important to note that the same approach can be used for classification in the presence of strain because the physical parameters used do not depend on strain. Although the magnitude of inter-layer energy can be expected to vary, we observed a negligible change in  $\Delta E_{ILE}$  threshold with strain (see Supplementary). Thus using these criterion based on ILS and ILE, we could classify atoms into their local stacking as shown in Fig. 2(f), which applies to TBGs with any twist angle and strain (Fig. 3(a)).

On implementing the classification method, we obtained area fractions ( $AF$ ) of each sub-domains present in a TBG structure. Using this measure to monitor the evolution of local domains in the presence of strain, we observed that the sub-domains'  $AF$  remain almost unchanged (Fig. 3(b), Fig. S4 for tension and Fig S5 for compression). It demonstrates a characteristic tendency of these local regions to retain their registry with an external strain applied globally. The variation of  $AF$  as a function of twist angle (Fig. 3(c)) shows that area fraction of AB ( $AF_{AB}$ ) and SP ( $AF_{SP}$ ) increases whereas that of AA ( $AF_{AA}$ ) decreases with decreasing  $\theta$ . This can be attributed to the potential energy of soliton (SP) regions contributing to in-plane forces, that displace atoms to maximize the area of AB/BA (most stable BLG-stacking) local domains<sup>30</sup>. Such observations are well-interpreted in experiments, particularly for systems close to  $\theta_m$  (1.08°). Hence we compared our theoretically estimated  $AF$  for  $\theta = 1.08^\circ$  (and additional  $\theta = 1.21^\circ, 1.37^\circ$ ) systems with experimentally interpreted area fractions from graphical analysis of STM images<sup>19</sup>, as marked in Fig. 3(c). The close similitude between these sets of area fraction values provides a validation of our stacking classification method. We believe our approach interprets the physical behavior of sub-domains at atomic-level and with high accuracy. Besides, as our method is based on physical parameters such as energy, it directly encapsulates the underlying physics while in contrast, the previously reported data rely on a graphical interpretation of gradient in image intensity and contrast from experiments. Hence, our methodology is more accurate and able to resolve atomistic insights even at a higher twist angle where the moiré cell size shrinks drastically.

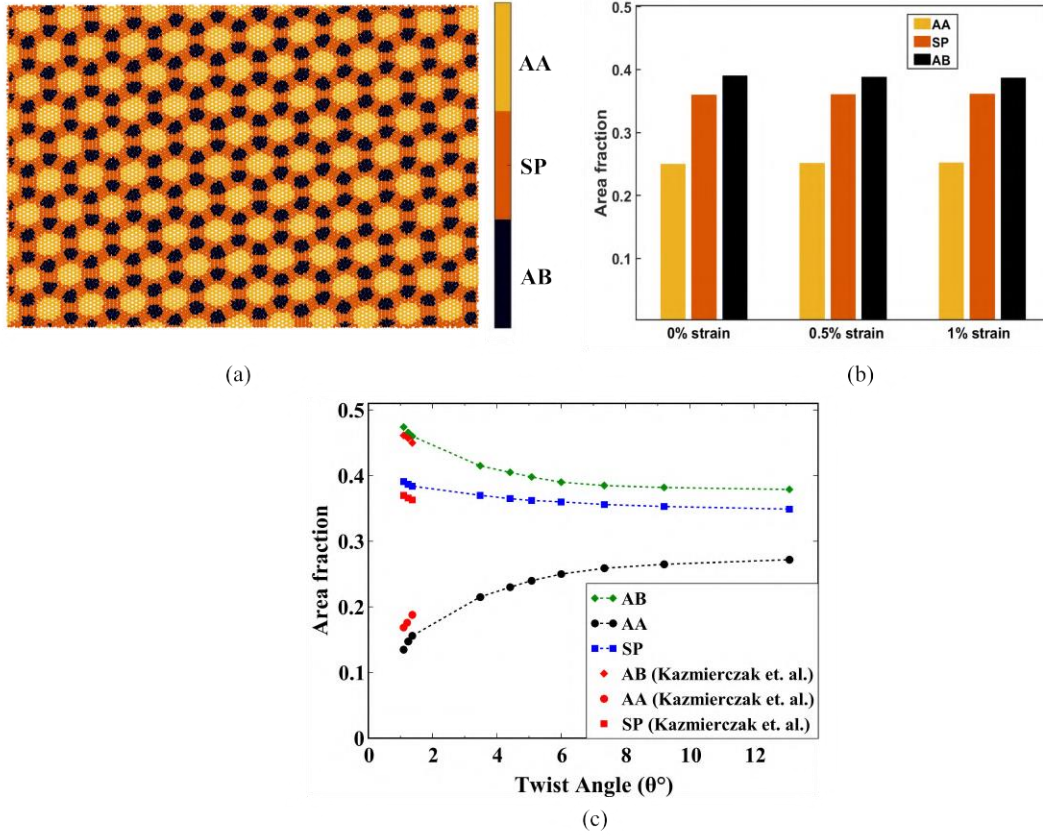


FIG. 3: **Evolution of local regions with twist angle and strain.** (a) Contour plot demonstrating local stacking type for heterostrained  $\theta = 6^\circ$  system (1% tension). Area fractions of individual stacking domain with respect to (b) strain (tension) and (c) twist angle. The red markings in (c) are extracted from reported work by Kazmierczak et. al.<sup>19</sup> to compare our results with data obtained by analyzing experimental measurements .

### C. Detecting moiré reconstruction in high twist angle TBGs.

We further utilized this method to study the extent of atomic reconstruction in TBG systems. Moiré reconstruction can be studied by examining local regions in rigidly twisted (R-TBG) structure and comparing with their relaxed geometry<sup>13–16</sup>. The rigidly twisted TBG refers to its unrelaxed geometry, considered in a conceptual intermediate configuration, in which the layers of BLG are twisted by a certain angle but the atoms are not allowed to reconfigure to form their true equilibrium structure. During reconstruction, local sites in the structure prefer to diverge from energetically unfavorable AA stacking by atomic displacements. This is achieved by rearrangement of the atoms to minimize vdW energy and obtaining the nearly commensurate Bernal-stacked (AB/BA) BLG structure partitioned by the SP segments after reconstruction. The emergence of soliton (SP) domains is one of the predominant features of reconstruction phenomena in 2D materials. Previous studies have attributed the minor atomic displacements of large  $\theta$  relaxed TBGs to insignificant change in atomic registry of local domains indicating the absence of reconstruction<sup>15–17,47</sup>. However, examining TBG systems with an atomistic insight and employing our sub-domain iden-

tification method, we show considerable changes in the local registries for larger  $\theta$  TBGs. We utilized the area fraction measure to capture the structural changes in local domains of relaxed and unrelaxed geometries. The stacking identification assessment of R-TBG is conducted similarly to the relaxed TBG (see Supplementary). For  $\theta = 6^\circ$  structure (4(a)-(c)), the AA regions shrink upon relaxation and conversely, the AB/BA regions expand to approximate triangular domains. Undoubtedly, this structural change was expected and prominently observed for  $\theta = 1.08^\circ$  system (4(d)-(f)). But we encountered a similar observation for a large  $\theta$  structure. Hence, contrary to the general idea that reconstruction diminishes at higher angles, we show clear evidence demonstrating moiré reconstruction in higher  $\theta$  ( $>2^\circ$ ) TBG systems. This observation indicates that irrespective of how small the atomic displacements are, the change in AF of local domains for higher  $\theta$  TBGs show pronounced variation in atomic registries upon relaxation.

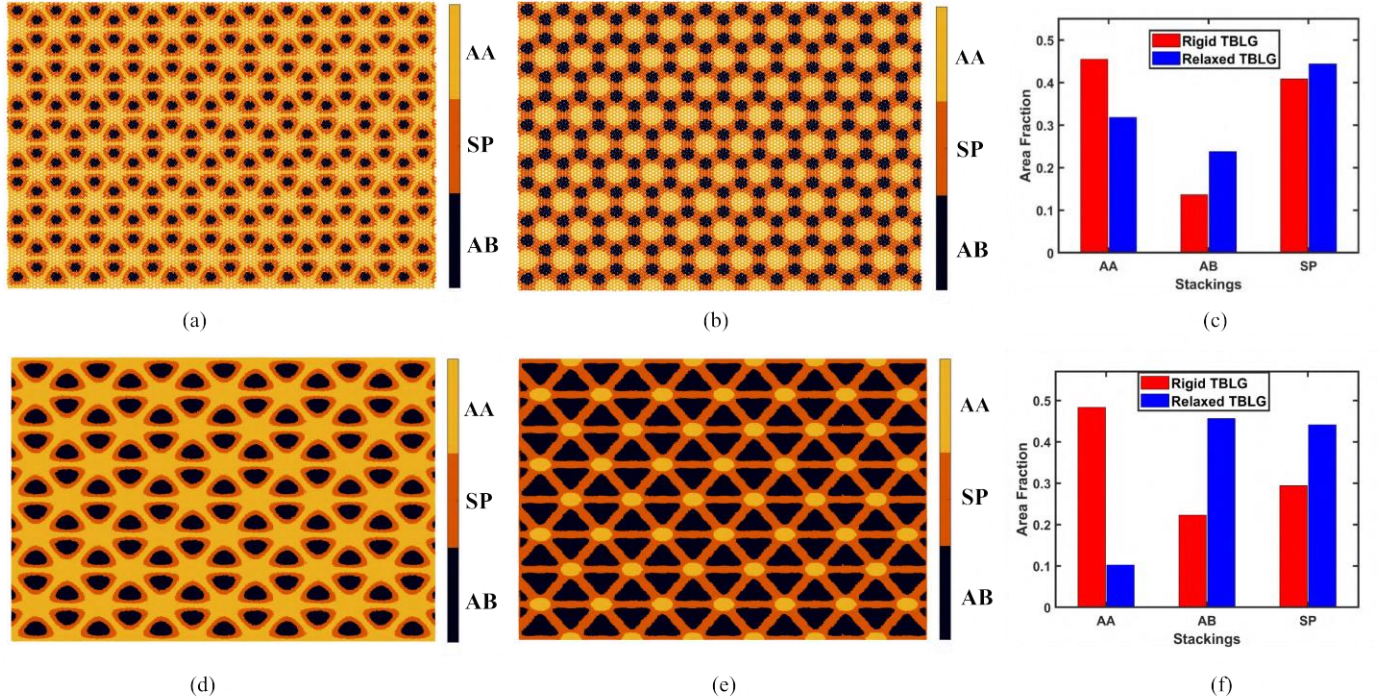


FIG. 4: **Demonstration of moiré reconstruction.** Stacking contour plot for rigid (a)  $\theta = 6^\circ$ , (d)  $\theta = 1.08^\circ$  and relaxed (b)  $\theta = 6^\circ$ , (e)  $\theta = 1.08^\circ$  TBG systems. (c), (f) Comparison of area fractions for each stacking, showing the change in local atomic registries before and after relaxation that signifies the extent of reconstruction.

#### D. Analyzing extent of reconstruction in strained and unstrained TBGs.

Using this approach, we have also studied the extent of moiré reconstruction in high angle TBGs in the presence of heterostrain. Lattice deformation due to heterostrain induces distortion in MPs, which is minimized by sustaining the formed domain-wall-like boundary lines (SP regions) due to superlattice reconstruction<sup>15,23,48</sup>. Similar to the unstrained case, we have compared the local  $AF$  of rigid and relaxed systems under heterostrain (Fig. 5). The rigid system for strained TBGs refers to its unrelaxed structure obtained after employing strain to the relaxed geometry of pristine TBG structure (see Supplementary). We observed that our assessment could capture the variations in local atomic registry of strained TBGs (Fig. 5(a)-(c)). The substantial change in  $AF$  of AA and AB regions and perpetual of SP domains, signifies the tendency of preserving the SP boundaries with change in local atomic registry of AA and AB domains, thus indicating the presence of atomic reconstruction in large  $\theta$  strained TBG systems. To assess the extent of change in local  $AF$  upon relaxing the structures, i.e.,  $\Delta AF(\%) = \left( \frac{AF_{relaxed} - AF_{rigid}}{AF_{rigid}} \right) \times 100$ . On examining the variation of  $\Delta AF$  over unstrained (Fig 5(c)) and strained (tensile Fig. 5(e) and compressive Fig. 5(f)) TBGs spanning a wide range of twist angles, it is observed that  $\Delta AF$  for all local stackings monotonically decreases with increasing  $\theta$ . Although this implies that, as expected, the ef-

fect of reconstruction reduces with increasing twist angle,  $AF$ s data shows that it can not be disregarded. It is noticed that for both pristine and strained cases, the AB stacked domains show ample variation in rigid and relaxed configurations even for higher angles. This variation rapidly decreases for AA and SP regions, especially at very high twist angles. Nonetheless, this analysis reveals the existence of local atomic reconstruction for both unstrained and strained large  $\theta$  TBG systems.

It has been previously argued that for a large twist angle, the gaining vdW energy cannot compensate for the losing intralayer elastic energy<sup>15,17,23</sup>. This results in no change of vdW stacking energy between rigid and relaxed structures, ultimately indicating the absence of reconstruction. However, our analysis of ILE over different  $\theta$  (Fig. S6) clearly shows a small but relatively significant difference between the rigid and relaxed structures of higher  $\theta$  TBGs. Although we observed a quick increase and gradual decrease in energies of relaxed and R-TBG respectively with increasing  $\theta$ , the relaxed (or reconstructed) system has the lower energy throughout. Thus, even for large twist angles the reconstructed structure formed as a consequence of local atomic changes is their energetically favorable configuration, which directly establishes the presence of reconstruction. It is not surprising that such minor changes in atomic registries for large twist angles are challenging to capture in experiments given the length scale limitations. But based on our results, reconstruction should not be neglected for higher angles and motivate the study of the implications of reconstruction for large  $\theta$  TBGs.



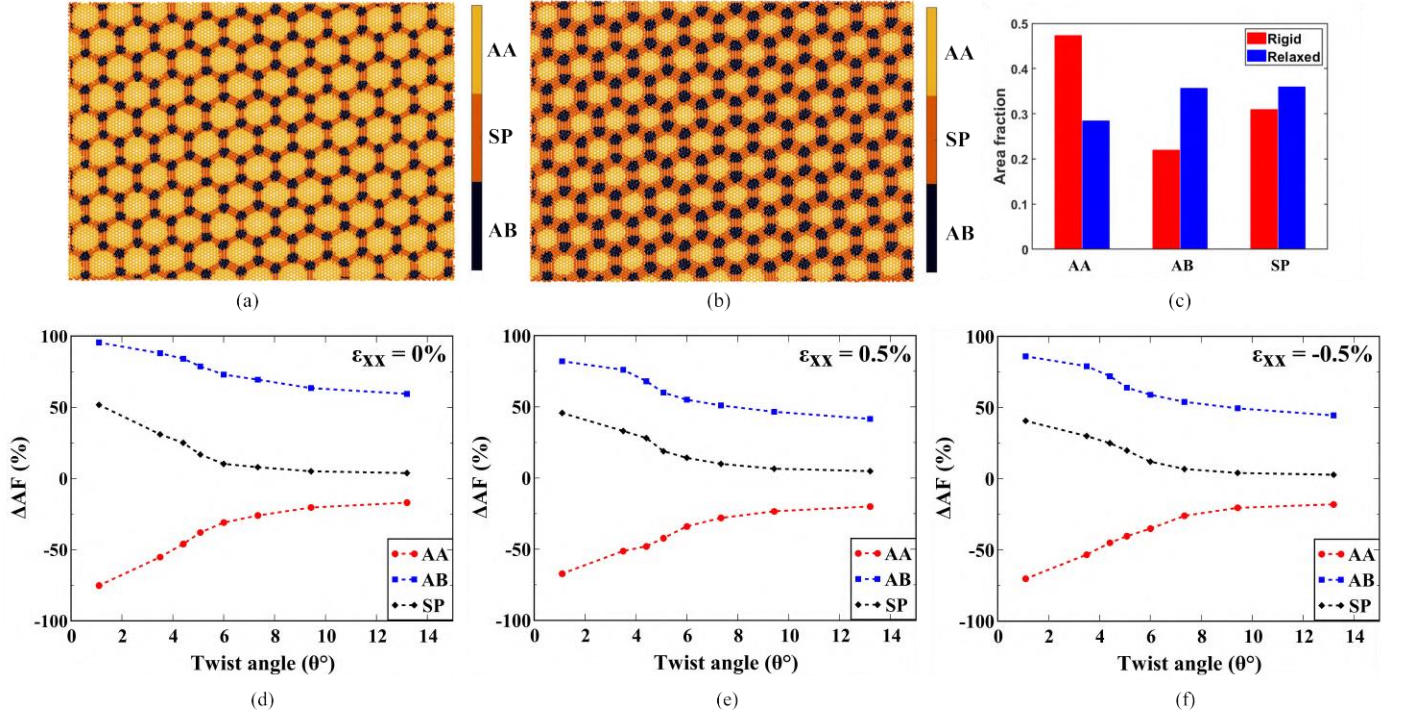


FIG. 5: **Moiré reconstruction in hetero-strained TBGs.** Stacking contour plot of (a) rigid and (b) relaxed  $\theta = 6^\circ$  structure in the presence of 0.5% uniaxial tension. (c) Change in local stacking area fractions before and after relaxation for the strained structure. Percentage change in local AF of rigid and relaxed  $\theta = 6^\circ$  structures ( $\Delta AF$ ) with respect to twist angle for (d) pristine (unstrained), (e) 1% strained (uniaxial tension) and (f) -1% strained (uniaxial compression) TBGs. Positive and negative values of  $\Delta AF$  (%) respectively indicates increase and decrease in respective local AFs

#### E. Mapping local and global physical property (phonon behavior) to changes in local atomic registry.

Further validation on the presence of reconstruction at high angles lies within an interrelation of local stacking domains and global vibrational properties. To accomplish this, we have studied their phonon behavior that can be directly translated to Raman scattering frequencies, which is an efficient experimental technique for examining these systems, especially under strain<sup>49–52</sup>. We have examined the phonon dispersion spectra of TBGs and their local domains with ab-initio simulations. Initially, we obtained the phonon spectra of unstrained TBG systems using DFT (See Methods and Supplementary). As compared to phonon spectrum of BLG, the difference in phonon modes for TBG is quite small due to weaker interlayer interaction (Fig. S7). Although we noticed some differences in low-frequency acoustic phonons, the effect is substantially feeble for optical modes that correspond to the experimentally observed Raman peaks<sup>53,54</sup>. Pertaining to our goal of probing Raman spectra of TBGs, we analyzed the high frequency optical (Longitudinal (LO) and Transverse (TO)) branches of its phonon spectra<sup>55</sup>. We have independently computed the phonon behavior of each sub-domain for comparing them to the global optical vibrational behavior (see Supplementary) as shown in Fig. 6(a). To analyze the minute difference between phonon frequencies of all the structures, we have plotted the optical phonon frequency difference ( $\Delta\omega$ )

of each stacking with respect to the whole TBG structure,  $\Delta\omega = \omega_{TBG} - \omega_{stacking}$  (Fig. 6(b) shows  $\Delta\omega$  for LO). We observed that the phonon frequency magnitude of AA and AB regions are smaller than TBG, whereas larger for SP region. A similar trend is observed while comparing the TO phonon modes (Fig. S8). The optical phonon behavior of AB stacking is the closest to that of TBG which indicates that AB-stacked domains predominantly control the overall phonon behavior in TBGs. This is because unfolded phonon branches of TBG exhibit an infinitesimal difference when compared to that of Bernal stacked BLG<sup>49,54</sup>. The correlation of AF measure with local and global phonon behavior is discussed in the following sub-sections.

##### 1. Correlating local area fraction measure and phonon behavior using Bond-Order-Length-Strength theory

To further establish a connection between the optical phonons modes of TBG and phonon frequencies of its sub-domains with individual stacking AF, we utilized the Bond Order Length Strength (BOLS) theory<sup>56</sup>. BOLS can correlate Raman peaks and their shifts in terms of constitutive structural parameters such as bond length and bond energy<sup>56–58</sup>. It explains that the intrinsic association of bonds with their physical properties can describe the extrinsic process of optical electron scattering captured by their phonon spectra. This theory provides an independent method of calculating phonon

frequencies of TBG based on the  $AF$ s of each sub-domain. Therefore, the comparison of the results from BOLS theory and ab-initio phonon frequencies of TBG can further validate the accuracy of our sub-domain categorizations. The details of BOLS formulation and the parameters involved are explained in Supplementary section I. To obtain the vibrational properties of various structures using BOLS correlation, we can deduce the phonon frequency shift based on bond length ( $d_z$ ), bond energy ( $E_z$ ), reduced mass ( $\mu$ ) and atomic coordination number ( $z$ ) using the following relation:

$$\Delta\omega \propto \frac{z}{d_z} \frac{E_z}{\mu} \quad (1)$$

$$\Delta\omega = k \frac{z}{d_z} \frac{E_z}{\mu} \quad (2)$$

$$\Delta\omega = \omega_{structure} - \omega_{bulk} = k(\beta) \quad (3)$$

where,  $k$  is the proportionality constant in Eq. 1 ( $\mu$  is constant because we have only carbon-based systems).  $\Delta\omega$  is the difference of the optical phonon frequency of a system and a reference material considered in bulk form (see Supplementary). Hence  $\Delta\omega = k\beta$ , where  $\beta$  is the pre-factor containing the variable parameters, such that  $\beta = \frac{z}{d_z} \frac{E_z}{\mu}$ . The magnitude of this pre-factor directly relates to the optical phonon frequency of a structure  $\omega_{structure}$ , and thus can help in calculating its phonon behavior in terms of the associated physical parameters (i.e.,  $z$ ,  $d_z$  and  $E_z$ ). Hence, we have utilized this BOLS theory based pre-factor  $\beta$  to study the phonon behavior of TBGs and their local domains, including their strained configurations.

The calculated  $\beta$  magnitudes for global TBG structure ( $\beta_{TBG}$ ) and its sub-domains are listed in Table I and values of all the parameters such as,  $d$ ,  $z$  and  $E$  are listed in Table SI. Although the  $\beta$  magnitudes are numerically close, they follow a trend as  $\beta_{SP} > \beta_{TBG} > \beta_{AB} > \beta_{AA}$ , on careful inspection. This trend also aligns with the observation made while comparing the optical frequencies of these structures (6(b)). Interestingly, this shows how effectively the BOLS theory could endorse the characteristic trend in their phonon behavior. Furthermore, we employed the local stacking  $AF$  values of reconstructed structures in BOLS expression to instill an alternate estimation of phonon frequencies in an attempt to authenticate our classification method, as explained hereon. We analyzed the phonon behavior of global TBG

structure based on two approaches, the first being  $\beta_{TBG}$  calculated directly from BOLS expression. For the other approach, we have taken a weighted average of  $\beta$  values of individual stacking with their reconstructed  $AF$  as the weights, i.e.,  $\beta_{TBG} = AF_{AA}\beta_{AA} + AF_{AB}\beta_{AB} + AF_{SP}\beta_{SP}$ . On comparing the actual and weighted  $\beta_{TBG}$ , i.e.,  $e_{actual} = (\beta_{TBG}^{(weighted)} - \beta_{TBG}^{(actual)}) / \beta_{TBG}^{(actual)}$ , we observed that they align very well with a small error % including for strained systems (Table II). However, given the seemingly small difference in  $\beta$

values of the structures, it may be argued that these small errors are not much intriguing. Therefore, we have additionally

TABLE I: List of  $\beta$  ( $eV^{1/2}\text{\AA}^{-1}$ ) pre-factor values

Stacking	$\theta = 1.08^\circ$	$\theta = 6^\circ$	$\theta = 13.2^\circ$
AA	3.084	3.198	3.418
AB	3.126	3.294	3.450
SP	3.180	3.376	3.491
TBG( $\beta_{BOLS}$ )	3.135	3.306	3.474
TBG( $\beta_{weighted}$ )	3.141	3.292	3.466

analyzed both the  $\beta_{TBG}$  values using a times improvement basis ( $m_i$ ). Using this we compared the weighted  $\beta_{TBG}$ , first by taking our calculated local reconstructed  $AF$  as the weights and second by randomly assigning equal  $AF$  (33.33% weight for three regions) to each individual stacking. We calculated their error % with actual  $\beta_{TBG}$  and obtained the relative error comparison or times improvement with respect to actual  $\beta_{TBG}$  values. The  $m_i$  values in Table II show significant times improvement on considering our estimated  $AF$  values of reconstructed structures. The similitude between global  $\beta_{TBG}$  and weighted  $\beta_{TBG}$  using local  $AF$ s signify that the physical attributes of local regions in a TBG structure directly correlate with the global vibrational compartment. Besides, this analysis shows another evidence that our stacking classification is an effective method for wide-ranging  $\theta$  and strain magnitudes, which is shown to detect reconstruction in these structures.

## 2. Comparison of BOLS-estimated phonon frequencies with experimental Raman to validate sub-domain area fraction measure

To authenticate our reconstructed  $AF$  measures with DFT-based phonon calculations and  $AF$ s driven BOLS theory, we first calculated the phonon spectra of strained TBGs using DFT simulations followed by calculating Raman frequencies using BOLS (see Supplementary). Figure 6(c) shows the optical phonon branches of TBG ( $\theta = 6^\circ$ ) including tensile and compressive uniaxial heterostrain. We have considered Raman G band frequency in this study, which can be obtained at  $\Gamma$  point in high symmetry Brillouin Zone path<sup>55,59</sup>. We observed strain-induced phonon band splitting due to inequivalent strain present in both the layers<sup>59-62</sup> (supplementary section IV). This phenomenon is observed in Raman spectroscopy as represented by the schematic of G-band Raman peaks in hetero-strained TBGs (Fig. 6(d)). Due to weak inter-layer vdW interaction in TBGs, their interlayer shear strength is negligible which results in slippage between the layers. Hence, the bottom layer remains mostly unstrained when straining the top layer<sup>62,63</sup>. The Raman spectra of heterostrained TBG show significant individual peaks of unstrained bottom layer ( $p_{\epsilon=0}^1$ ) and strained top layer ( $p_{\epsilon=\pm 1\%}^{2'}$ ). The peak of strained layer redshifts or blueshifts depending on the nature of strain. Also, for the case of graphene, an increase in the magnitude of strain further splits the G-band peaks corresponding to the doubly degenerate  $E_{2g}^+$  and  $E_{2g}^-$  phonons ( $p_{\epsilon=\pm 1\%}^2$  in Fig 6(d)-(f))<sup>8,64</sup>.  $AF$  values of reconstructed systems

We then used the local  $AF$  values of reconstructed systems in BOLS expression to estimate Raman G-band frequencies for comparison with experiments. and establish a connec-



TABLE II: Error table for BOLS-estimated  $\beta$  pre-factors based on actual and weighted  $\beta_{TBG}$ , for systems with and without strain.

Strain (%)	$\theta = 1.08^\circ$		$\theta = 6^\circ$		$\theta = 13.2^\circ$	
	$e_{actual}$	$m_i$	$e_{actual}$	$m_i$	$e_{actual}$	$m_i$
0	0.38	6	0.27	5	0.22	5
0.2%	-	-	0.42	5	0.29	4
0.5%	-	-	0.60	5	0.35	4
0.7%	-	-	0.51	5	0.49	4
1%	-	-	0.69	5	0.45	3

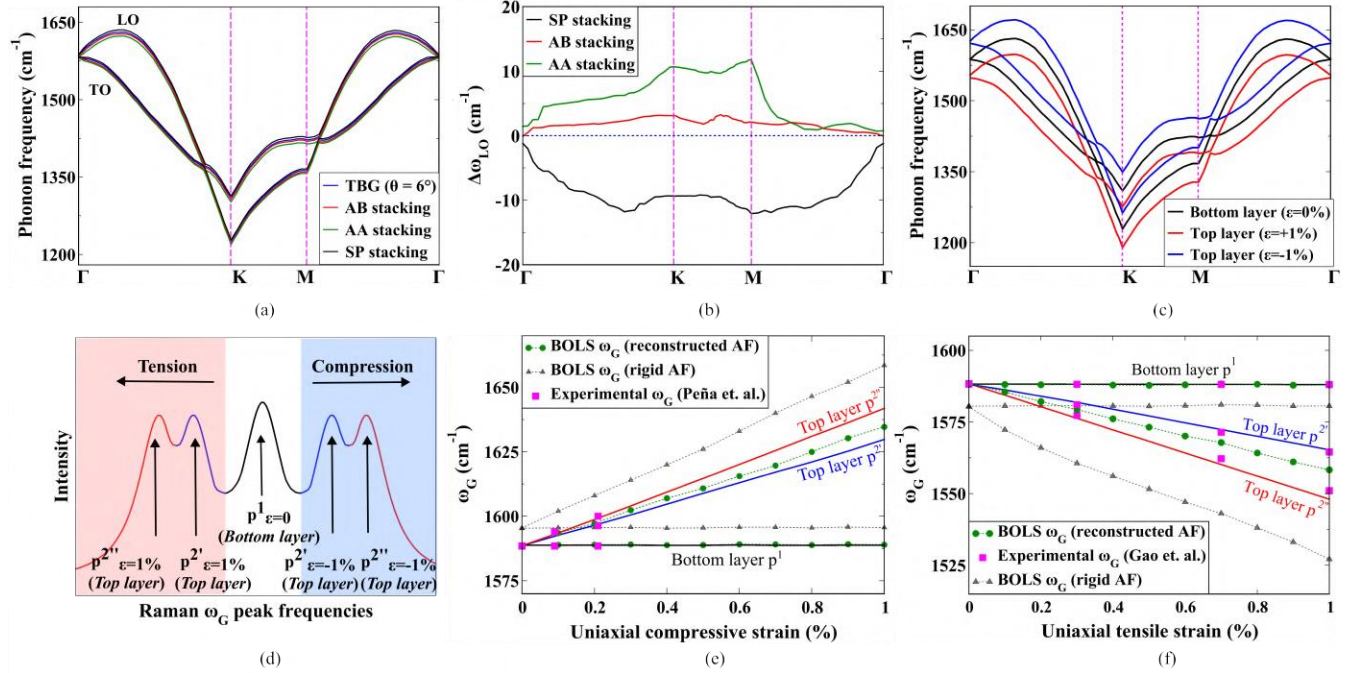


FIG. 6: **Phonon behavior of TBGs with respect to its local domains.** (a) Optical phonon modes of TBLG ( $\theta = 6^\circ$ ) and its individual counterparts. (b) Longitudinal optical (LO) phonon frequency difference with respect to TBG system, (c) Phonon band splitting with heterostrain (tension and compression) (d) Schematic of a typical Raman G-peak splitting with inequivalent strain employed in a bilayer system. Comparison of G-band frequencies for (e)  $\theta = 6^\circ$  with uniaxial compression and (f)  $\theta = 13.2^\circ$  with uniaxial tension. Solid lines in (e), (f) denote the Raman G-peak data obtained from DFT-based phonon calculations. Heterostrain-assisted peak splitting of top and bottom layer (as shown in the schematic) is also denoted. Sub-figures(e)-(f) also shows the close alignment of Bond Order Length Strength (BOLS)-estimated data using reconstructed AFs with DFT-calculated and experimental data (reported by Peña et. al.<sup>65</sup>) as compared to that using rigid TBG AFs.

tion between global and local vibrational behavior. We first extracted the G-band frequency ( $\omega_G$ ) from DFT-simulated phonon spectra for both unstrained and strained structures. Figure 6(e) and 6(f) respectively shows the variation of  $\omega_G$  for  $6^\circ$  and  $13.2^\circ$  with strain. To demonstrate both directions of uniaxial strain, we showed the case of compression for  $6^\circ$  and tension for  $13.2^\circ$ . In both cases, we observed that  $\omega_G$  at zero strain is  $1588 \text{ cm}^{-1}$ , which changes negligibly for the unstrained bottom layer. In Fig. 6(e) due to compression, we observed blueshift in  $\omega_G$  and redshift for tensile strain in Fig. 6(f) (see Supplementary section V). On comparing our results for  $6^\circ$  and  $13.2^\circ$  systems with the experimental data reported by Pena et. al.<sup>65</sup> and Gao et. al.<sup>8</sup> respectively, we found a good agreement between them (magenta data points in Fig.

6(e) and (f)). Finally, to achieve an experimental validation of our stacking identification method as well as to highlight that the global behavior such as Raman scattering is tied to local structural configurations, we used our calculated AFs of reconstructed TBGs in BOLS to predict the Raman G-band frequencies of heterostrained systems (see Supplementary section I for details).

We found a qualitative agreement between BOLS estimated and DFT calculated  $\omega_G$  Raman peaks shown in Fig. 6(e) and Fig. 6(f) (green dots). It must be noted that since BOLS approach encompasses mathematical interpolation for projecting the phonon frequencies, it can not resolve the further band splitting of the strained top layer. We have also used the rigid TBG AFs to check how it compares with the estimated G-

band frequencies. We observed a distinct misalignment of BOLS-estimated Raman data using rigid *AFs* with that using reconstructed *AFs* and experimentally obtained data as well. Hence, our analysis clearly demonstrates the difference in vibrational behavior of reconstructed and rigid structures and also shows that the reconstructed systems align closely with the experimentally obtained measurements. This certainly implies that the physical behavior of TBGs such as their vibrational properties is governed by their reconstructed phases even for a large  $\theta$  system and hence establishes an additional validation on the presence of moiré reconstruction in their structures. Moreover, an agreement between the *AF* utilized BOLS-estimated Raman data and DFT-calculated phonon shows a theoretical approach to calculate Raman frequencies at a comparatively lower computational cost. We have calculated the G-band data for the heterostrained  $1.08^\circ$  system using BOLS formulation (Fig. S9). As a whole utilizing our stacking classification method and analyzing their Raman signature using BOLS, we established a precise authentication about reconstruction in high twist angles and also demonstrated a connection of the global phonon shift of a TBG system with changes in its local atomic registries.

#### IV. Conclusion

Using atomistic simulations, we studied the characteristics of locally stacked domains in TBG moiré patterns and demonstrated a comprehensive approach to study atomic reconstruction phenomena in these structures, including the presence of heterostrain. We proposed a way to classify TBGs into their stacking types (AA, AB, and SP) and calculated their area fractions to track structural evolution as a function of  $\theta$  and strain. Our classification scheme allowed us to exhibit the existence of moiré reconstruction even for larger twist angle ( $>2^\circ$ ) TBG systems, which is difficult to detect experimentally. We showed how the moiré patterns of these large-angle TBGs can be distorted by applying strain. Besides, the atomic reconstruction in the presence of strain (in terms of area fraction change of commensurate domain) can be manipulated by an amount between 55% to 73% (for  $\theta = 6^\circ$ ) with an applied strain of only 0.5%, opening up a massive opportunity for large angle TBGs to be used in strain engineering applications.

We studied the extent of reconstruction over a wide range of  $\theta$  and realized how it evolves in the presence of strain. To further analyze this finding and validate the *AF* measure, we utilized DFT-based phonon calculations and a theoretical approach (BOLS theory) to deduce Raman frequencies and compare them with experimental data. Using BOLS theory, we discovered that global phonon behavior is directly related to the physical features of local regions. Further, we realized that the Raman data using reconstructed *AFs* in BOLS aligns closely with DFT-calculated as well as experimental data. Moreover, on comparing the Raman data with rigid *AFs*, our results show a clear difference with that using the reconstructed sub-domains and hence imply that the latter governs the physical behavior in TBGs even for higher angles. Hence, our study shows a self-consistent approach to characterize local regions in TBGs and utilize them to examine as well as

validate moiré reconstruction phenomena, based on physical measures. Our findings on the presence of reconstruction in large  $\theta$  TBGs might open up an interesting research outlook in twistrionics. Moreover, our methodologies can be utilized to identify stacking types and perform similar analyses in other twisted vdW systems, especially in the presence of strain.

#### Acknowledgments

We wish to acknowledge the support from the National Science Foundation (OMA-1936250) and National Science Foundation Graduate Research Fellowship Program (DGE-1939268).

#### Data Availability Statement

The data that support the findings of this study are available from the corresponding author upon reasonable request.

#### References

- <sup>1</sup>X.-J. Zhao, H. Hou, X.-T. Fan, Y. Wang, Y.-M. Liu, C. Tang, S.-H. Liu, P.-P. Ding, J. Cheng, D.-H. Lin, *et al.*, “Molecular bilayer graphene,” *Nature communications* **10**, 1–7 (2019).
- <sup>2</sup>K. Lee, B. Fallahazad, J. Xue, D. C. Dillen, K. Kim, T. Taniguchi, K. Watanabe, and E. Tutuc, “Chemical potential and quantum hall ferromagnetism in bilayer graphene,” *Science* **345**, 58–61 (2014).
- <sup>3</sup>T. Ohta, A. Bostwick, T. Seyller, K. Horn, and E. Rotenberg, “Controlling the electronic structure of bilayer graphene,” *Science* **313**, 951–954 (2006).
- <sup>4</sup>E. McCann and M. Koshino, “The electronic properties of bilayer graphene,” *Reports on Progress in physics* **76**, 056503 (2013).
- <sup>5</sup>A. Luican, G. Li, A. Reina, J. Kong, R. Nair, K. S. Novoselov, A. K. Geim, and E. Andrei, “Single-layer behavior and its breakdown in twisted graphene layers,” *Physical review letters* **106**, 126802 (2011).
- <sup>6</sup>A. Luican, G. Li, A. Reina, J. Kong, R. R. Nair, K. S. Novoselov, A. K. Geim, and E. Y. Andrei, “Single-layer behavior and its breakdown in twisted graphene layers,” *Phys. Rev. Lett.* **106**, 126802 (2011).
- <sup>7</sup>Y. Yu, K. Zhang, H. Parks, M. Babar, S. Carr, I. M. Craig, M. Van Winkle, A. Lyssenko, T. Taniguchi, K. Watanabe, *et al.*, “Tunable angle-dependent electrochemistry at twisted bilayer graphene with moiré flat bands,” *Nature Chemistry* **14**, 267–273 (2022).
- <sup>8</sup>X. Gao, H. Sun, D.-H. Kang, C. Wang, Q. J. Wang, and D. Nam, “Heterostrain-enabled dynamically tunable moiré superlattice in twisted bilayer graphene,” *Scientific reports* **11**, 1–8 (2021).
- <sup>9</sup>L. Huder, A. Artaud, T. Le Quang, G. T. De Laissardiere, A. G. Jansen, G. Lapertot, C. Chapelier, and V. T. Renard, “Electronic spectrum of twisted graphene layers under heterostrain,” *Physical review letters* **120**, 156405 (2018).
- <sup>10</sup>J.-B. Qiao, L.-J. Yin, and L. He, “Twisted graphene bilayer around the first magic angle engineered by heterostrain,” *Physical Review B* **98**, 235402 (2018).
- <sup>11</sup>F. Gargiulo and O. V. Yazyev, “Structural and electronic transformation in low-angle twisted bilayer graphene,” *2D Materials* **5**, 015019 (2017).
- <sup>12</sup>N. N. Nam and M. Koshino, “Lattice relaxation and energy band modulation in twisted bilayer graphene,” *Physical Review B* **96**, 075311 (2017).
- <sup>13</sup>K. Zhang and E. B. Tadmor, “Structural and electron diffraction scaling of twisted graphene bilayers,” *Journal of the Mechanics and Physics of Solids* **112**, 225–238 (2018).
- <sup>14</sup>Y.-W. Liu, Y. Su, X.-F. Zhou, L.-J. Yin, C. Yan, S.-Y. Li, W. Yan, S. Han, Z.-Q. Fu, Y. Zhang, Q. Yang, Y.-N. Ren, and L. He, “Tunable lattice reconstruction, triangular network of chiral one-dimensional states, and band-width of flat bands in magic angle twisted bilayer graphene,” *Phys. Rev. Lett.* **125**, 236102 (2020).
- <sup>15</sup>H. Yoo, R. Engelke, S. Carr, S. Fang, K. Zhang, P. Cazeaux, S. H. Sung, R. Hovden, A. W. Tsen, T. Taniguchi, *et al.*, “Atomic and electronic reconstruction at the van der waals interface in twisted bilayer graphene,” *Nature materials* **18**, 448–453 (2019).

- <sup>16</sup>Y. Choi, J. Kemmer, Y. Peng, A. Thomson, H. Arora, R. Polski, Y. Zhang, H. Ren, J. Alicea, G. Refael, *et al.*, “Electronic correlations in twisted bilayer graphene near the magic angle,” *Nature Physics* **15**, 1174–1180 (2019).
- <sup>17</sup>T. A. de Jong, T. Benschop, X. Chen, E. E. Krasovskii, M. J. de Dood, R. M. Tromp, M. P. Allan, and S. J. Van der Molen, “Imaging moiré deformation and dynamics in twisted bilayer graphene,” *Nature Communications* **13**, 1–8 (2022).
- <sup>18</sup>A. C. Gadelha, D. A. Ohlberg, C. Rabelo, E. G. Neto, T. L. Vasconcelos, J. L. Campos, J. S. Lemos, V. Ornelas, D. Miranda, R. Nadas, *et al.*, “Localization of lattice dynamics in low-angle twisted bilayer graphene,” *Nature* **590**, 405–409 (2021).
- <sup>19</sup>N. P. Kazmierczak, M. Van Winkle, C. Ophus, K. C. Bustillo, S. Carr, H. G. Brown, J. Ciston, T. Taniguchi, K. Watanabe, and D. K. Bediako, “Strain fields in twisted bilayer graphene,” *Nature materials* **20**, 956–963 (2021).
- <sup>20</sup>T. C. Barbosa, A. C. Gadelha, D. A. Ohlberg, K. Watanabe, T. Taniguchi, G. Medeiros-Ribeiro, A. Jorio, and L. C. Campos, “Raman spectra of twisted bilayer graphene close to the magic angle,” *2D Materials* **9**, 025007 (2022).
- <sup>21</sup>Z.-B. Dai, Y. He, and Z. Li, “Effects of heterostrain and lattice relaxation on the optical conductivity of twisted bilayer graphene,” *Phys. Rev. B* **104**, 045403 (2021).
- <sup>22</sup>L. Zhang, Y. Wang, R. Hu, P. Wan, O. Zheliuk, M. Liang, X. Peng, Y.-J. Zeng, and J. Ye, “Correlated states in strained twisted bilayer graphenes away from the magic angle,” *Nano letters* **22**, 3204–3211 (2022).
- <sup>23</sup>A. Kerelsky, L. J. McGilly, D. M. Kennes, L. Xian, M. Yankowitz, S. Chen, K. Watanabe, T. Taniguchi, J. Hone, C. Dean, *et al.*, “Maximized electron interactions at the magic angle in twisted bilayer graphene,” *Nature* **572**, 95–100 (2019).
- <sup>24</sup>J. Campos-Delgado, G. Algara-Siller, C. Santos, U. Kaiser, and J.-P. Raskin, “Twisted bi-layer graphene: Microscopic rainbows,” *Small* **9**, 3247–3251 (2013).
- <sup>25</sup>Y. Wang, Z. Su, W. Wu, S. Nie, N. Xie, H. Gong, Y. Guo, J. Hwan Lee, S. Xing, X. Lu, *et al.*, “Resonance raman spectroscopy of g-line and folded phonons in twisted bilayer graphene with large rotation angles,” *Applied Physics Letters* **103**, 123101 (2013).
- <sup>26</sup>A. Jorio and L. G. Cançado, “Raman spectroscopy of twisted bilayer graphene,” *Solid State Communications* **175**, 3–12 (2013).
- <sup>27</sup>J. Campos-Delgado, L. G. Cançado, C. A. Achete, A. Jorio, and J.-P. Raskin, “Raman scattering study of the phonon dispersion in twisted bilayer graphene,” *Nano Research* **6**, 269–274 (2013).
- <sup>28</sup>R. He, T.-F. Chung, C. Delaney, C. Keiser, L. A. Jauregui, P. M. Shand, C. Chancey, Y. Wang, J. Bao, and Y. P. Chen, “Observation of low energy raman modes in twisted bilayer graphene,” *Nano letters* **13**, 3594–3601 (2013).
- <sup>29</sup>M. Koshino and Y.-W. Son, “Moiré phonons in twisted bilayer graphene,” *Physical Review B* **100**, 075416 (2019).
- <sup>30</sup>S. Dai, Y. Xiang, and D. J. Srolovitz, “Twisted bilayer graphene: Moiré with a twist,” *Nano letters* **16**, 5923–5927 (2016).
- <sup>31</sup>M. Koshino, “Electronic transmission through a b-b a domain boundary in bilayer graphene,” *Physical Review B* **88**, 115409 (2013).
- <sup>32</sup>M. Van Wijk, A. Schuring, M. Katsnelson, and A. Fasolino, “Relaxation of moiré patterns for slightly misaligned identical lattices: graphene on graphite,” *2D Materials* **2**, 034010 (2015).
- <sup>33</sup>V. Carozo, C. M. Almeida, E. H. Ferreira, L. G. Cancado, C. A. Achete, and A. Jorio, “Raman signature of graphene superlattices,” *Nano letters* **11**, 4527–4534 (2011).
- <sup>34</sup>W. Hou, S. A. Chowdhury, A. Dey, C. Watson, T. Peña, A. Azizmanesh, H. Askari, and S. M. Wu, “Nonvolatile ferroelastic strain from flexoelectric internal bias engineering,” *Physical Review Applied* **17**, 024013 (2022).
- <sup>35</sup>P. Kumar, A. Dey, J. Roques, L. Assaud, S. Franger, P. Parida, and V. Biju, “Photoexfoliation synthesis of 2d materials,” *ACS Materials Letters* **4**, 263–270 (2022).
- <sup>36</sup>V. Kumar, A. Dey, S. Thomas, M. A. Zaeem, and D. R. Roy, “Hydrogen-induced tunable electronic and optical properties of a two-dimensional penta-pt 2 n 4 monolayer,” *Physical Chemistry Chemical Physics* **23**, 10409–10417 (2021).
- <sup>37</sup>A. Dey, R. Sharma, and S. A. Dar, “An extensive investigation of structural, electronic, thermoelectric and optical properties of bi-based half-huesler alloys by first principles calculations,” *Materials Today Communications* **25**, 101647 (2020).
- <sup>38</sup>A. Dey, B. A. Baraiya, S. Adhikary, and P. K. Jha, “First-principles calculations of the effects of edge functionalization and size on the band gap of be3n2 nanoribbons: Implications for nanoelectronic devices,” *ACS Applied Nano Materials* **4**, 493–502 (2020).
- <sup>39</sup>A. P. Thompson, H. M. Aktulga, R. Berger, D. S. Bolintineanu, W. M. Brown, P. S. Crozier, P. J. in’t Veld, A. Kohlmeyer, S. G. Moore, T. D. Nguyen, *et al.*, “Lammps-a flexible simulation tool for particle-based materials modeling at the atomic, meso, and continuum scales,” *Computer Physics Communications* **271**, 108171 (2022).
- <sup>40</sup>S. A. Chowdhury, K. Inzani, T. Peña, A. Dey, S. M. Wu, S. M. Griffin, and H. Askari, “Mechanical properties and strain transfer behavior of molybdenum ditelluride (mote2) thin films,” *Journal of Engineering Materials and Technology* **144** (2022).
- <sup>41</sup>L. J. McGilly, A. Kerelsky, N. R. Finney, K. Shapovalov, E.-M. Shih, A. Ghiotto, Y. Zeng, S. L. Moore, W. Wu, Y. Bai, *et al.*, “Visualization of moiré superlattices,” *Nature Nanotechnology* **15**, 580–584 (2020).
- <sup>42</sup>J. Lin, W. Fang, W. Zhou, A. R. Lupini, J. C. Idrobo, J. Kong, S. J. Pennycook, and S. T. Pantelides, “Ac/ab stacking boundaries in bilayer graphene,” *Nano letters* **13**, 3262–3268 (2013).
- <sup>43</sup>X. Lin, D. Liu, and D. Tománek, “Shear instability in twisted bilayer graphene,” *Physical Review B* **98**, 195432 (2018).
- <sup>44</sup>L. Gong, R. J. Young, I. A. Kinloch, S. J. Haigh, J. H. Warner, J. A. Hinks, Z. Xu, L. Li, F. Ding, I. Riaz, *et al.*, “Reversible loss of bernal stacking during the deformation of few-layer graphene in nanocomposites,” *Acs Nano* **7**, 7287–7294 (2013).
- <sup>45</sup>R. Miwa, P. Venezuela, and E. S. Morell, “Periodic arrays of intercalated atoms in twisted bilayer graphene: An ab initio investigation,” *Physical Review B* **92**, 115419 (2015).
- <sup>46</sup>Y. Hou, S. Zhang, Q. Li, L. Liu, X. Wu, and Z. Zhang, “Evaluation local strain of twisted bilayer graphene via moiré pattern,” *Optics and Lasers in Engineering* **152**, 106946 (2022).
- <sup>47</sup>M. Koshino and N. N. Nam, “Effective continuum model for relaxed twisted bilayer graphene and moiré electron-phonon interaction,” *Physical Review B* **101**, 195425 (2020).
- <sup>48</sup>L. Zhang, Y. Wang, R. Hu, P. Wan, O. Zheliuk, M. Liang, X. Peng, Y.-J. Zeng, and J. Ye, “Correlated states in strained twisted bilayer graphenes away from the magic angle,” *Nano Letters* **22**, 3204–3211 (2022), pMID: 35385281, <https://doi.org/10.1021/acs.nanolett.1c04400>.
- <sup>49</sup>F. Wu, A. H. MacDonald, and I. Martin, “Theory of phonon-mediated superconductivity in twisted bilayer graphene,” *Physical review letters* **121**, 257001 (2018).
- <sup>50</sup>R. W. Havener, H. Zhuang, L. Brown, R. G. Hennig, and J. Park, “Angle-resolved raman imaging of interlayer rotations and interactions in twisted bilayer graphene,” *Nano letters* **12**, 3162–3167 (2012).
- <sup>51</sup>A. C. Gadelha, D. A. Ohlberg, F. C. Santana, G. S. Eliel, J. S. Lemos, V. Ornelas, D. Miranda, R. B. Nadas, K. Watanabe, T. Taniguchi, *et al.*, “Twisted bilayer graphene: a versatile fabrication method and the detection of variable nanometric strain caused by twist-angle disorder,” *ACS Applied Nano Materials* **4**, 1858–1866 (2021).
- <sup>52</sup>M. Huang, H. Yan, T. F. Heinz, and J. Hone, “Probing strain-induced electronic structure change in graphene by raman spectroscopy,” *Nano letters* **10**, 4074–4079 (2010).
- <sup>53</sup>A. I. Cocemasov, D. L. Nika, and A. A. Balandin, “Phonons in twisted bilayer graphene,” *Physical Review B* **88**, 035428 (2013).
- <sup>54</sup>M. Lamparski, B. Van Troeye, and V. Meunier, “Soliton signature in the phonon spectrum of twisted bilayer graphene,” *2D Materials* **7**, 025050 (2020).
- <sup>55</sup>H. Wang, Y. Wang, X. Cao, M. Feng, and G. Lan, “Vibrational properties of graphene and graphene layers,” *Journal of Raman Spectroscopy: An International Journal for Original Work in all Aspects of Raman Spectroscopy, Including Higher Order Processes, and also Brillouin and Rayleigh Scattering* **40**, 1791–1796 (2009).
- <sup>56</sup>X. Yang, Y. Wang, J. Li, W. Liao, Y. Liu, and C. Q. Sun, “Graphene phonon softening and splitting by directional straining,” *Applied Physics Letters* **107**, 203105 (2015).
- <sup>57</sup>C. Q. Sun, “Size dependence of nanostructures: Impact of bond order deficiency,” *Progress in solid state chemistry* **35**, 1–159 (2007).
- <sup>58</sup>C. Q. Sun, “Relaxation of the chemical bond,” *Springer Ser. Chem. Phys* **108**, 807 (2014).



- <sup>59</sup>D. Yoon, Y.-W. Son, and H. Cheong, “Strain-dependent splitting of the double-resonance raman scattering band in graphene,” *Physical review letters* **106**, 155502 (2011).
- <sup>60</sup>O. Frank, M. Bousa, I. Riaz, R. Jalil, K. S. Novoselov, G. Tsoukleri, J. Parthenios, L. Kavan, K. Papagelis, and C. Galiotis, “Phonon and structural changes in deformed bernal stacked bilayer graphene,” *Nano Letters* **12**, 687–693 (2012).
- <sup>61</sup>T. Sohler, M. Gibertini, M. Calandra, F. Mauri, and N. Marzari, “Breakdown of optical phonons’ splitting in two-dimensional materials,” *Nano letters* **17**, 3758–3763 (2017).
- <sup>62</sup>C. Androulidakis, E. N. Koukaras, G. Paterakis, G. Trakakis, and C. Galiotis, “Tunable macroscale structural superlubricity in two-layer graphene via strain engineering,” *Nature communications* **11**, 1–11 (2020).
- <sup>63</sup>K. Wang, C. Qu, J. Wang, W. Ouyang, M. Ma, and Q. Zheng, “Strain engineering modulates graphene interlayer friction by moiré pattern evolution,” *ACS applied materials & interfaces* **11**, 36169–36176 (2019).
- <sup>64</sup>Y. Lu, L. Yan, S. Hussain, M. Sun, Z. Zhang, and H. Zheng, “Interlayer coulomb interaction in twisted bilayer graphene nanofragments characterized by the vibrational mode of gr+ band,” *Applied Physics Letters* **120**, 083103 (2022).
- <sup>65</sup>T. Peña, A. Dey, S. A. Chowdhury, A. Azizimanesh, W. Hou, A. Sewaket, C. L. Watson, H. Askari, and S. M. Wu, “Moiré engineering in 2d heterostructures with process-induced strain,” *arXiv* (2022).
- <sup>66</sup>Y. Cao, V. Fatemi, S. Fang, K. Watanabe, T. Taniguchi, E. Kaxiras, and P. Jarillo-Herrero, “Unconventional superconductivity in magic-angle graphene superlattices,” *Nature* **556**, 43–50 (2018).
- <sup>67</sup>A. Nimbalkar and H. Kim, “Opportunities and challenges in twisted bilayer graphene: a review,” *Nano-Micro Letters* **12**, 1–20 (2020).

# An atomistic insight to moiré reconstruction in Twisted Bilayer Graphene beyond magic angle

Aditya Dey,<sup>1, a)</sup> Shoieb Ahmed Chowdhury,<sup>1, a)</sup> Tara Peña,<sup>2</sup> Sobhit Singh,<sup>1</sup> Stephen M. Wu,<sup>2, b)</sup> and Hesam Askari<sup>1</sup>

<sup>1)</sup>*Department of Mechanical Engineering, University of Rochester,  
New York*

<sup>2)</sup>*Department of Electrical and Computer Engineering, University of Rochester,  
Rochester, New York*

## Supplementary information

---

<sup>a)</sup>These authors contributed equally to this work

<sup>b)</sup>Department of Physics and Astronomy, University of Rochester, Rochester, New York

## I. COMPUTATIONAL AND THEORETICAL METHODS

### A. DFT calculations

The real space lattices of TBG systems were constructed using ATOMISTIX TOOLKIT (QuantumATK) commercial package. All the first principles simulations were conducted with generalized gradient approximation (GGA)<sup>1,2</sup> assimilated in Quantum Espresso open source package. The Perdew-Burke-Ernzerhof (PBE) form along with GGA has been used as the exchange-correlation functional<sup>3</sup>. Ion-electron interactions for carbon atoms in TBGs have been described by ultrasoft pseudopotentials. The vdW interaction has been incorporated as well using the semi-empirical Grimme functional<sup>4</sup>. Wavefunctions are expanded using a plane wave basis set with an energy cutoff and charge density of 55 Ry and 450 Ry respectively. We used  $14 \times 14 \times 1$  k-point grid within Monkhorst-Pack<sup>5,6</sup> scheme to sample the reciprocal space Brillouin zone. The structures were optimized until all the atomic forces were less than  $0.01 \text{ eV}/\text{\AA}$ . The in-plane lattice constants were relaxed including the non-periodic out-of plane lattice ( $25 \text{ \AA}$  space) to elude interactions in that direction. Phonon dispersion spectra of all TBG structures were simulated using self-consistent density functional perturbation theory (DFPT)<sup>7,8</sup>. The dynamical matrices were first computed on an adequate q-point grid. The inter-atomic constants used in computing the phonon dispersion were obtained from the Fourier interpolation of these dynamical matrices.

### B. MS simulations

Molecular statics simulations were done using LAMMPS open source software. The unstrained, DFT-relaxed TBG moiré lattice was transformed into an orthogonal cell with approximate dimensions of  $32 \text{ nm} \times 20 \text{ nm}$  for all the TBG structures. The number of MPs generated in each structure is dependent on the twist angle, for example  $\theta = 6^\circ$  has 72 MPs, and  $\theta = 13.2^\circ$  has 288 MPs respectively. A vacuum space of  $50 \text{ \AA}$  is inserted along the out-plane-direction to avoid interactions with the periodic images. Hydrogen passivation was done along the free surfaces to obtain the most stable structure. The TBG structures were minimized using a conjugate gradient energy minimization method to have minimum energy configurations. A reactive empirical bond order (REBO) potential was used for the intra-layer covalent bonds<sup>9</sup> and for the interlayer van der Waals interaction a registry-dependent



Kolmogorov-Crespi (KC) potential<sup>10</sup> was selected. As TBG contains different local stacking configurations, an interatomic potential that considers registry different than equilibrium minimum energy stacking is needed<sup>11,12</sup>. Subsequently, we loaded the structure with constant incremental strain to the top layer. We limit the magnitude of applied strain to 1% for impeding our analysis within the contended boundaries of the experimental capability of straining such systems<sup>13,14</sup>. Between each loading step, the atoms of the top layer were kept stationary at the applied strain level and energy minimization was performed. The snapshots of the structure at different strain magnitudes were taken in Ovito open visualization tool<sup>15</sup>.

### C. BOLS formulation

The BOLS notion explains the bond contraction and bond strengthening phenomena using the following expressions<sup>16</sup>:

$$\frac{d_z}{d_b} = C_z = \frac{2}{1 + \exp\left[\frac{12-z}{8z}\right]} \quad (1)$$

$$E_z = \frac{E_b}{C_z^m} \quad (2)$$

Here, the subscripts  $z$  and  $b$  respectively represent the coordination number (CN) of a particular atomic structure and its bulk counterpart as a standard. The terms  $d$  and  $E$  denote bond length and bond energy respectively.  $C_z$  represents the bond contraction coefficient that varies with atomic structures having different  $z$ . The bond nature index is denoted by  $m$  which is 2.56 for carbon bonds<sup>17</sup>. Since we are dealing with graphitic structures in this study, we consider the bulk counterpart as diamond. Using the bond length of the diamond ( $d_b = 1.54 \text{ \AA}$ ) and bond lengths  $d_z$  for each stacking configuration, we can calculate  $C_z$  and  $z$  for each configuration using equations (1) and (2). Again using the relation given in equation (2), we can calculate the bond energy for each individual stacking. For diamond, the single C-C bond energy can be obtained from its total cohesive energy, which is known to us, i.e.,  $E_b = 0.614 \text{ eV}$ <sup>17</sup>. Having known  $z$ ,  $d_z$  and  $E_z$ , we calculate the  $\beta$  pre-factor values for each stacking using equation (2). The relation stated in equation 1 in the main text can be derived by equating the vibrational energy of a harmonic system to the first-order approximated Taylor series of its interatomic potential as<sup>16</sup>:

$$\frac{1}{2}\mu(\Delta\omega)^2x^2 \cong \frac{1}{2}\frac{\delta u(r)}{\delta r^2}x^2 \propto \frac{1}{2}\frac{E_z}{d_z^2}x^2 \quad (3)$$

$$\Rightarrow \Delta\omega \propto \frac{z}{d_z} \frac{E_z}{\mu}$$

The BOLS correlation is also used to estimate the phonon frequencies pertaining to Raman G-band peaks. To achieve this, we perform some steps of mathematical interpolation for equation (3). We can write the equation as  $\Delta\omega^G = \omega_{TBG}^G - \omega_{ref}^G = k(\beta)$ , where  $\omega_{ref}^G$  is the G band frequency of any reference material. Now we can calculate  $\omega_{ref}^G$  for each TBG system with respect to their bulk counterpart (diamond) by comparing respective  $\beta$  pre-factors as,  $\frac{\omega_{TBG}^G - \omega_{ref}^G}{\omega_{diamond} - \omega_{ref}^G} = \frac{\beta_{TBG}}{\beta_{diamond}}$ . After obtaining  $\omega_{ref}^G$ , we can exercise  $\omega_{TBG}^{G,\epsilon=0}$  ( $\omega_{TBG}^G$  at zero strain) and  $\beta$  pre-factors of strained and unstrained TBG systems to estimate their G-band frequency in strained configuration ( $\omega_{TBG}^{G,\epsilon}$ ), as  $\frac{\omega_{TBG}^{G,\epsilon=0} - \omega_{ref}^G}{\omega_{TBG}^{G,\epsilon} - \omega_{ref}^G} = \frac{\beta_{TBG}^{\epsilon=0}}{\beta_{TBG}^\epsilon}$ . Operating this individually for top and bottom layers, we can obtain their G-peak frequencies for both directions and various magnitudes of applied strain. The  $\beta_{TBG}^\epsilon$  values for the strained top layer are listed in Table SIV. Since the bottom layer remains unstrained, we observe negligible differences between their  $\beta$  pre-factor values for strained and unstrained configurations.

## II. GEOMETRIC ANALYSIS OF STRAINED MSCS

We deduce the expressions of their reciprocal lattice ( $\vec{q}$ ) vectors to quantify the structural changes in strained MSCs<sup>18,19</sup>. The reciprocal lattice vectors of TBG moiré lattices<sup>20</sup> ( $\vec{q}$ ) is given as  $\vec{q} = \vec{b}' - \vec{b}$ , where  $\vec{b}'$  and  $\vec{b}$  denote the reciprocal lattice vectors of the rotated top layer and bottom layer in a TBG structure respectively. The length of moiré pattern (MP),  $L_m$  can be derived using the magnitude of  $\vec{q}$  vector as  $L_m = \frac{4\pi}{3|\vec{q}|}$ . When strain is applied to the top layer, the mathematical expression of its reciprocal lattice vector<sup>19</sup> ( $b_i^{\vec{\epsilon}}$ ) can be written as  $b_i^{\vec{\epsilon}} = (\Gamma + \vec{S})^{-1} \vec{b}_i$ , where  $\Gamma$  is the identity matrix and  $\vec{S}$  denotes the strain tensor which can be written as the following for the case of uniaxial tension,

$$\vec{S} = \begin{pmatrix} \epsilon & 0 \\ 0 & -\nu\epsilon \end{pmatrix}$$

Here,  $\epsilon$  is the nominal strain applied and  $\nu$  denotes the Poisson's ratio. So, the reciprocal lattice vector of TBG with heterostrain can be expressed as  $b_i^{\vec{\epsilon}} = b_i^{\vec{\epsilon}} - b_i$ . As shown in

Fig 1(e) in the main text, the boundaries of MPs resemble a hexagon and we can draw a triangle ( $\Delta ABC$ ) with  $\vec{A}B$  and  $\vec{B}C$  as the MP lattice vectors and  $\alpha$  being the angle between them ( $\alpha = 60^\circ$ ,  $\phi = 120^\circ$ ). The variation of  $\alpha$  and  $\phi$  with the applied strain is shown in Fig. S2. With uniaxial tension, we see a monotonic decrease in these angles and vice-versa for uniaxial compression. The changes in expressions of  $\vec{q}$  vectors are associated with the geometrical changes enforced upon hetero-straining these systems.

### III. EXPLANATION OF STACKING IDENTIFICATION METHOD (FOR UNSTRAINED AND STRAINED SYSTEMS)

Firstly, we performed the identification of atoms that should be classified as 'AA' type using ILS. As observed in main text Fig. 1(c) and (d), the spacing between two layers of TBG varies due to out-of-plane displacements of atoms. The ILS of equilibrium structures follows this trend:  $AA > SP > AB$ . Hence, in a TBG system, the maximum ILS ( $d_{max}$ ) corresponds to AA region and the minimum distance ( $d_{min}$ ) represents AB region. It is observed that  $d_{max}$  and  $d_{min}$  vary with increasing twist angle up to  $21^\circ$ , after which we noticed a plateaued regime<sup>21</sup>. This results due to the depletion of perfectly stacked AA and AB configurations, as the length of the MPs, reduces with increasing  $\theta$ . We obtained the maximum and minimum magnitudes of  $d_{max}$  ( $3.589 \text{ \AA}$  and  $3.475 \text{ \AA}$ ) and  $d_{min}$  ( $3.456 \text{ \AA}$  and  $3.338 \text{ \AA}$ ). Using the lower bound of  $d_{max}$  for all the twist angles, i.e.,  $3.475 \text{ \AA}$ , we classified the atoms with local ILS greater than  $3.475 \text{ \AA}$  as 'AA' stacking type. On the other hand, considering the upper bound of  $d_{min}$  and identifying the regions with ILS below that value as AB stacking can lead to the misclassification of AB and SP types. For the wide range of twist angle considered in this study, the ILS alone cannot provide a margin of separation for classifying AB and SP stacked atoms. To address this issue, we considered interlayer energy or ILE (per atom) in the structure. Perusing the ILE contour plot, we observed that the center of MPs has the highest energy followed by the SP segments. The AB (or BA) has the lowest energy corresponding to the ground state configuration of BLG. But, being a per atom quantity, the C atoms in AB stacking that are present directly on top of a C atom on the other layer show the highest ILE value as shown in main text Fig. 2(c).

To obtain the same measure of energy for AB stacked atoms whether they are located at the center of a lattice hexagon or at the corner, we calculated the difference of interlayer



energy of each atom with its three bonded neighbors and consider their average. The interlayer energy difference with neighboring atoms allows us to easily classify AB stacked atoms as they have the highest fluctuation of energy with neighbors compared to AA or SP stacked regions where the quantity is quite uniform. To obtain a classification threshold of interlayer energy difference for AB stacking, we first calculated the soliton width of different TBG systems, i.e., the width of SP regions similarly as explained by Gargiulo et al<sup>21</sup>. On analyzing the path from the center of AB domain to the center of another AB (or BA) region, we traverse across the SP segment. Calculating the ILS and plotting it along the centers of triangular (AB) regions, we observed a small peak (Fig S3). This peak corresponds to the SP region and its full width at half maxima (FWHM) gives us the soliton width<sup>21</sup>. Considering this soliton width (varies with twist angle), we obtained the interlayer energy difference value at the boundary of SP domains. This process is repeated for different twist angles to establish a unique threshold that can be applied to any TBG system. The energy difference threshold lies in a diminutive range, 8.22-8.31 meV for the angles considered (Fig 2(e) in main text). On averaging these magnitudes, we defined a  $\Delta E_{ILE}$  threshold of 8.24 meV/atom, above which an atom is classified as AB stacking type. The contour plot of TBG ( $\theta = 6^\circ$ ) system in main Fig 2(f) shows the outcome of applying the method where each atom has been classified as belonging to either AA or AB or SP stacked. We utilized the same approach for classifying the local domains in strained systems. Since the ILS parameter defines the out-of-plane distancing of pristine structures, it is not affected by an in-plane applied strain. However, the interlayer energy of the structure is expected to change because an externally applied strain disturbs the interlayer interactions. But since the mechanical deformation is applied globally, the local regions will experience a similar change in ILE with respect to their nearest neighbors and hence  $\Delta E_{ILE}$  remains approximately unchanged (see Table S1).

#### IV. STACKING IDENTIFICATION OF RIGID STRUCTURES

We followed the same approach used for reconstructed or relaxed systems to classify local regions in rigid structures. The atomistic structure of rigid TBGs (R-TBGs) is different from reconstructed systems. Since they are created by simply employing a rigid twist to a Bernal stacked bilayer graphene, they do not have a variation of interlayer spacing, which is

present in reconstructed TBGs pertaining to the formation of local stackings in the structure. When a R-TBG is modeled from Bernal stacked (or AB) graphene, it has an ILS equal to that of AB stacked graphene throughout its structure. Hence to account for this we defined their uniform ILS, which is different from their initial geometry. We first considered their relaxed structure and obtained an average ILS value considering all the interlayer distances throughout the structure. Then, we re-modeled the rigid TBG structure by adjusting the layers with respect to the average ILS value. Since different structures have varying fractions of local interlayer regions, this average ILS changes for systems with certain twist angles. It must be noted that we have not utilized this average ILS to define any threshold to classify local atoms, rather it is used only to define the respective rigid structures. Further, following the same method as relaxed systems we obtained their interlayer energy followed by calculating the ILE difference ( $\Delta E_{ILE}$ ) per atom. Now to classify the individual stackings, we referred back to the ILS and  $\Delta E_{ILE}$  thresholds obtained for relaxed systems. Having known the ILS threshold for AA region ( $3.475 \text{ \AA}$ ), we then identified the  $\Delta E_{ILE}$  value at the location corresponding to that ILS value by traversing along path PQ (Fig. 2(a) main text). Then, we employed this value in  $\Delta E_{ILE}$  calculation for R-TBG and specified atoms above that threshold ( $6.88 \text{ meV/atom}$ ) as AA. For identifying AB type, we have considered the  $\Delta E_{ILE}$  threshold ( $8.24 \text{ meV/atom}$ ) corresponding to its location on the path PQ. Similarly, we then used that location to detect  $\Delta E_{ILE}$  threshold for AB type in R-TBG structure ( $5.92 \text{ meV/atom}$ , so it lies between  $5.92$  and  $6.88 \text{ meV/atom}$ ). After classifying AB and AA, we have assigned the remaining atoms as SP. Further, we have used this same method to identify the local stackings in rigid structures of strained configurations. To model rigid systems of strained TBGs in a way that physically makes sense, we first considered the relaxed or reconstructed structure of pristine TBG. Now the top layer is stretched such that an unrelaxed hetero-strained TBG system is generated, which is referred to as the rigid structure in the presence of strain. Relaxing this strained structure results in a fully optimized system, pertaining to the reconstructed TBG configuration with strain.

## V. PHONON DISPERSION SPECTRA OF TBG AND ITS LOCAL DOMAINS

The simulations for phonon dispersion spectra were performed for  $\theta = 6^\circ$  and  $13.2^\circ$  systems. Due to the computational cost of DFT-based phonon simulations for large MPs, we computed phonon spectra only for  $\theta > 4.41^\circ$  systems. We discussed an approach using BOLS correlation to predict the Raman peaks pertaining to optical phonon modes for larger TBG systems. As described by Cocemasov et al, TBGs contain hybrid folded phonon branches that require to be unfolded onto the single layer first BZ<sup>22</sup>. Using the PhononUnfolding package<sup>23</sup>, we simplified the phonon spectra of TBGs along  $\Gamma$ -K-M- $\Gamma$  high symmetry path (Fig S7 shows unfolded spectra of  $\theta = 6^\circ$ ). To obtain the phonon spectra of local sub-domains, we first identified the atomic positions of each local stacking as defined by our identification method and extract the data from the main structure. Then, we calculated the average bond length  $l_{avg}$  of each configuration and deduce their respective lattice constant as  $a_{stacking} = \sqrt{3}l_{avg}$ . With the calculated unit cell parameters, we have computed their phonon spectrum.

## VI. PHONON BAND SPLITTING WITH HETEROOSTRAIN

A combination of Molecular statics and first principles simulations has been used to compute phonon dispersion spectra of TBGs with heterostrain. By freezing the obtained configuration from LAMMPS, we have extracted the atomic data of strained periodic moiré lattice and further minimized the supercell in DFT to obtain first-principles-level fidelity, followed by phonon spectra calculations. We observed strain-induced phonon band splitting due to inequivalent strain present in both layers. With tension, the atomic bonds in a crystal are stretched relative to their unstrained condition. When the bond length is increased, and the force constant remains unchanged, as a result, the vibrational frequency decreases. Conversely for compression, the bond length reduces which leads to an increase in vibrational frequency. That is why we observe redshift and blueshift in phonon frequencies for tensile and compressive strain respectively<sup>24</sup>. The redshift and blueshift of Raman G-band for  $\theta = 1.08^\circ$ , shown in Fig. S9 is a good demonstration of this phenomenon.

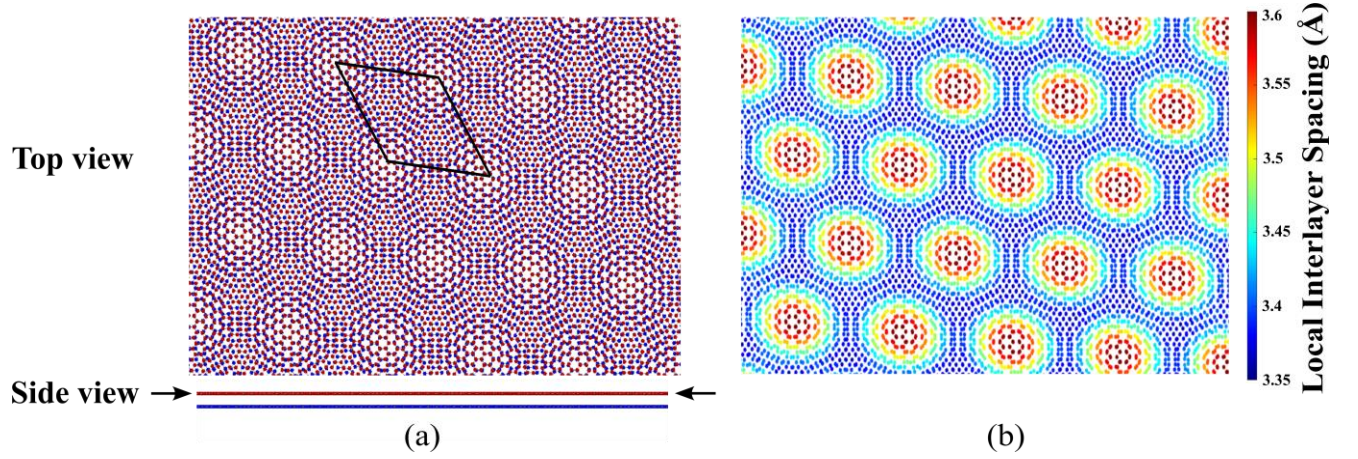


FIG. 1: (a) Relaxed atomistic structure and (b) interlayer spacing contour plot of  $\theta = 6^\circ$  TBG system under 1% uniaxial compressive strain.

TABLE I: Average  $\Delta E_{ILE}$  threshold value considering five representative TBG systems ( $\theta = 1.1^\circ, 3.48^\circ, 4.41^\circ, 6^\circ$  and  $7.34^\circ$ ) in the presence of strain.

Strain (%)	$\Delta E_{ILE}$ (meV/atom)
0	8.24
+0.5	8.223
-0.5	8.21
+1	8.23
-1	8.207



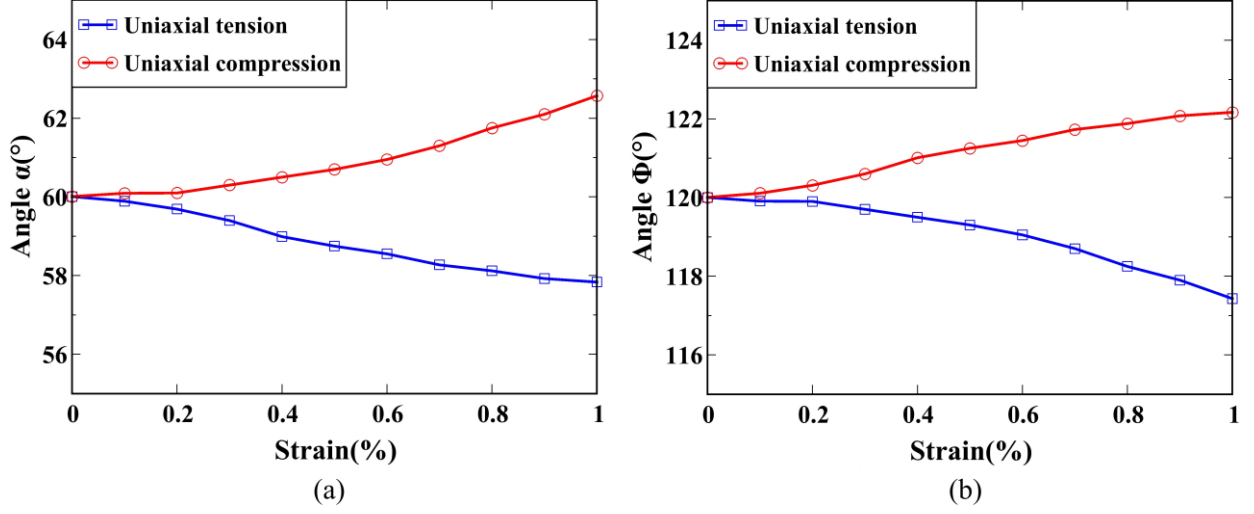


FIG. 2: Variation of angles  $\alpha$  and  $\phi$  with strain demonstrating the deformation of moiré patterns (for TBG system  $\theta = 6^\circ$ )

TABLE II: Evolution of area fractions  $f$  of local stacking domains with uniaxial tension and compression applied to the top layer

Strain (%)	$\theta = 1.1^\circ$			$\theta = 6^\circ$			$\theta = 13.2^\circ$		
	$f_{AA}$	$f_{AB}$	$f_{SP}$	$f_{AA}$	$f_{AB}$	$f_{SP}$	$f_{AA}$	$f_{AB}$	$f_{SP}$
0	0.135	0.474	0.391	0.25	0.39	0.36	0.272	0.379	0.349
+0.2	-	-	-	0.261	0.376	0.363	0.293	0.338	0.369
-0.2	-	-	-	0.239	0.407	0.354	0.257	0.399	0.344
+0.5	-	-	-	0.274	0.356	0.37	0.309	0.317	0.374
-0.5	-	-	-	0.218	0.432	0.35	0.239	0.419	0.342
+0.7	-	-	-	0.289	0.339	0.372	0.322	0.301	0.377
-0.7	-	-	-	0.2	0.455	0.345	0.218	0.443	0.339
+1	-	-	-	0.302	0.319	0.379	0.330	0.291	0.379
-1	-	-	-	0.188	0.471	0.341	0.2	0.462	0.338

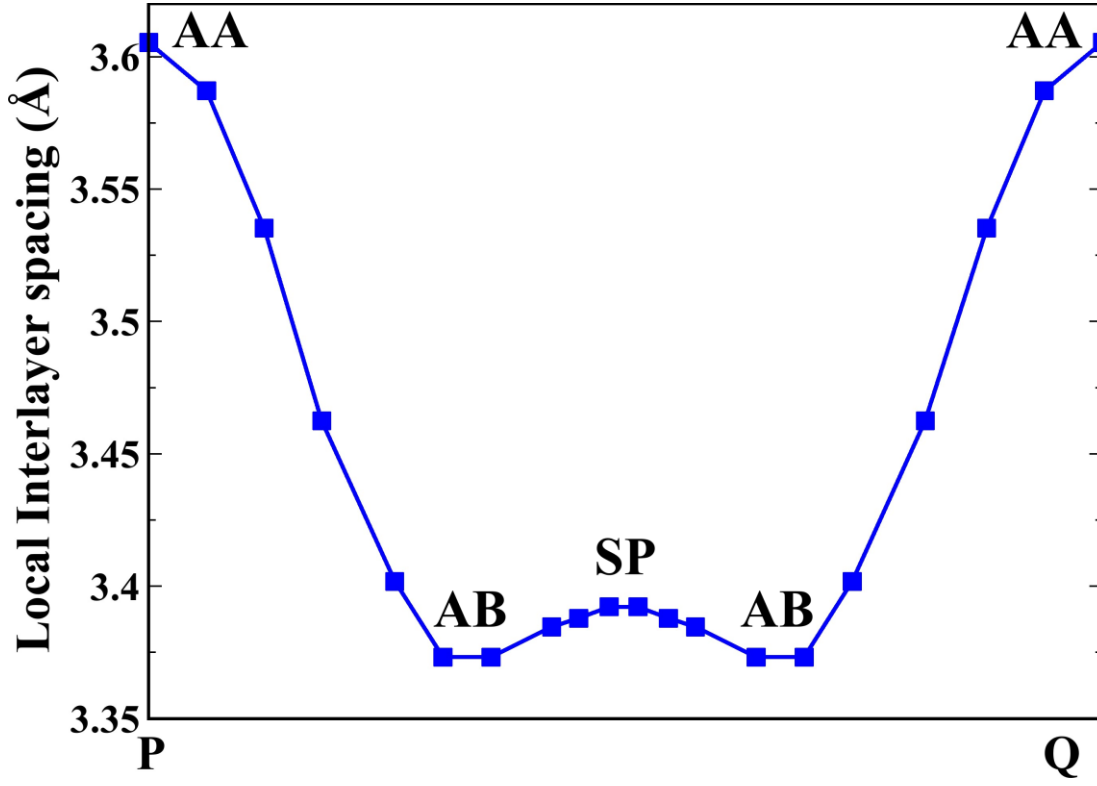


FIG. 3: Normalized spatial interlayer spacing difference ( $\Delta d$ ) profiles traversing between centers of moiré pattern, i.e., path PQ in Fig. 2(a) (for TBG system  $\theta = 6^\circ$ )

TABLE III: Parameters for calculating  $\beta_{BOLS}$  pre-factors for TBGs and their respective sub-domains.

Parameters	$\theta = 1.1^\circ$				$\theta = 6^\circ$				$\theta = 13.2^\circ$			
	TBG	AA	AB	SP	TBG	AA	AB	SP	TBG	AA	AB	SP
$d_z$ (Å)	1.406	1.40	1.405	1.411	1.424	1.417	1.423	1.43	1.438	1.431	1.437	1.441
$z$	5.008	4.88	4.987	5.12	5.43	5.185	5.409	5.612	5.851	5.67	5.792	5.911
$C_z$	0.913	0.909	0.912	0.916	0.926	0.918	0.924	0.929	0.933	0.929	0.933	0.935
$E_z$ (eV)	0.775	0.783	0.776	0.768	0.752	0.764	0.751	0.741	0.73	0.743	0.733	0.727

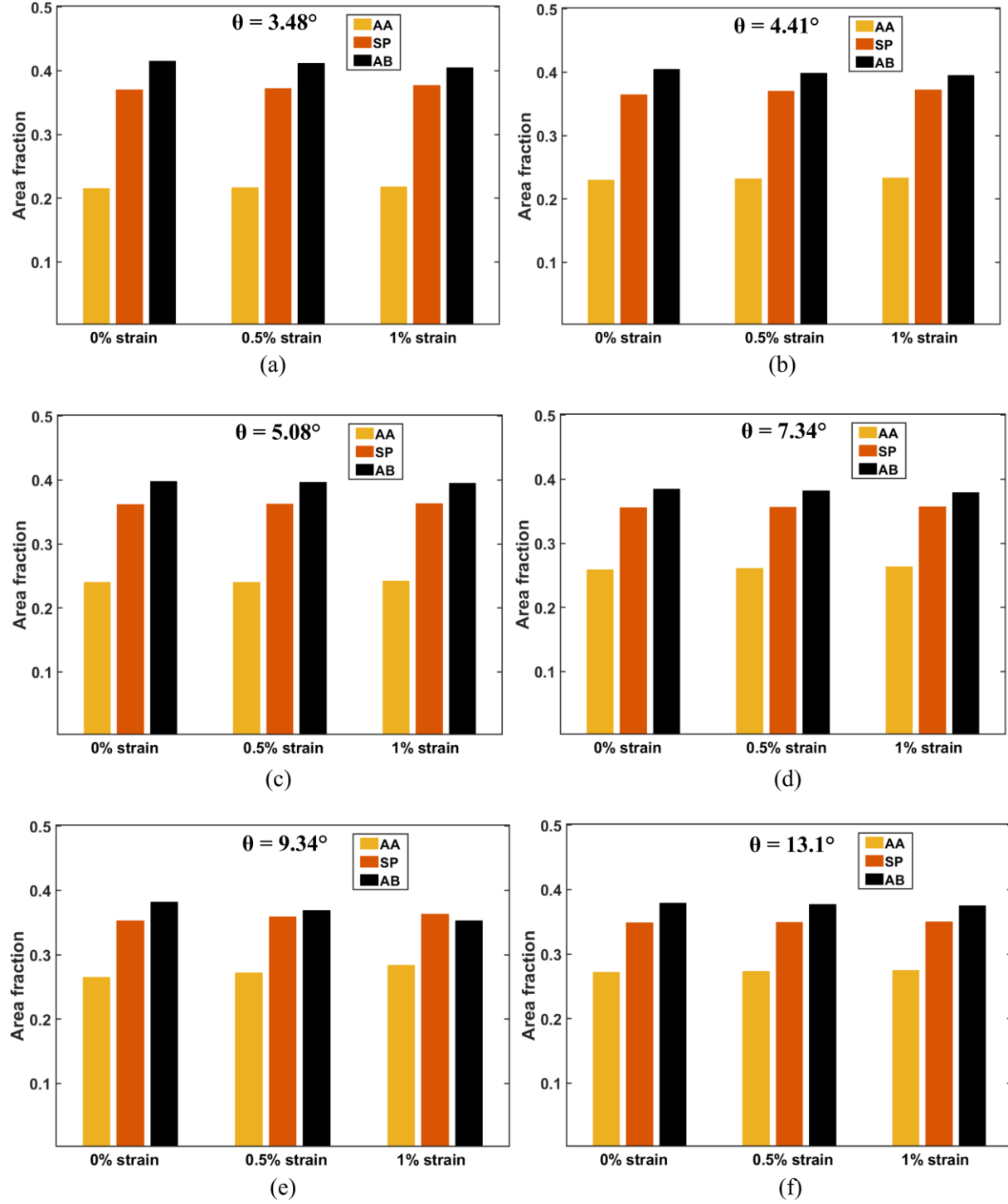


FIG. 4: Variation of area fractions of individual stacking domain with respect to heterostrain (tension) for different twist angles

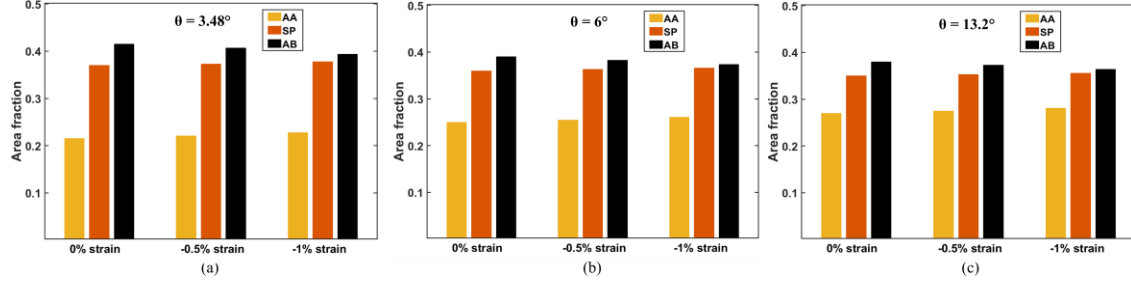


FIG. 5: Variation of area fractions of individual stacking domain with respect to heterostrain (compression) for  $\theta = 3.48^\circ$ ,  $6^\circ$  and  $13.2^\circ$

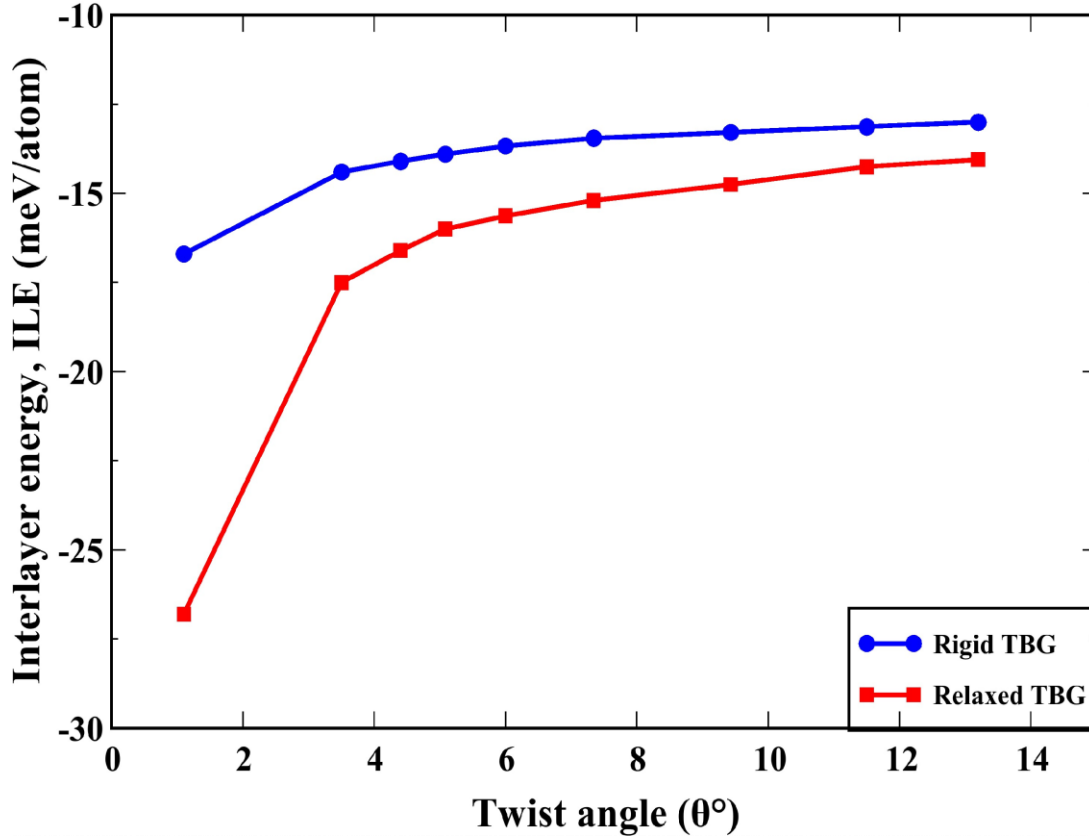


FIG. 6: Interlayer energy or vdW stacking energy for rigid and relaxed TBG systems. The ILE of relaxed TBG system is always lower than rigid TBG even for larger twist angles.

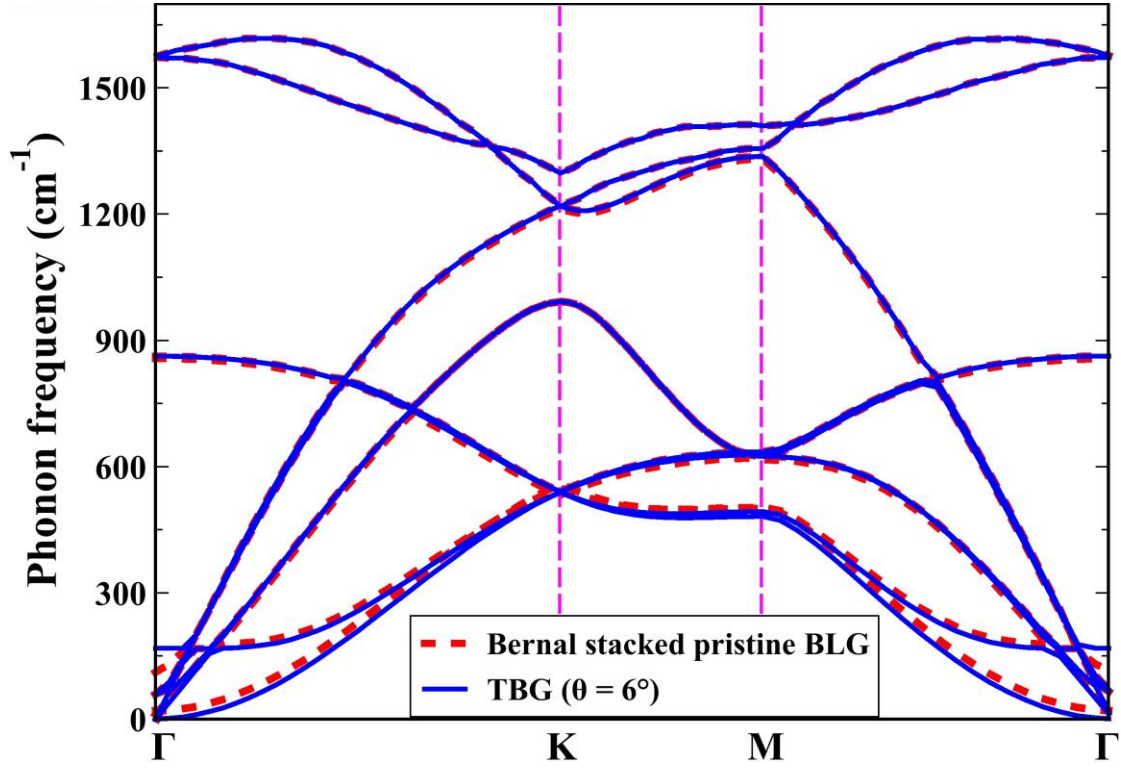


FIG. 7: Unfolded phonon spectra of TBG system  $\theta = 6^\circ$  along high symmetry points of its Brillouin zone. Phonon dispersion spectra of Bernal stacked BLG is also shown for comparison.



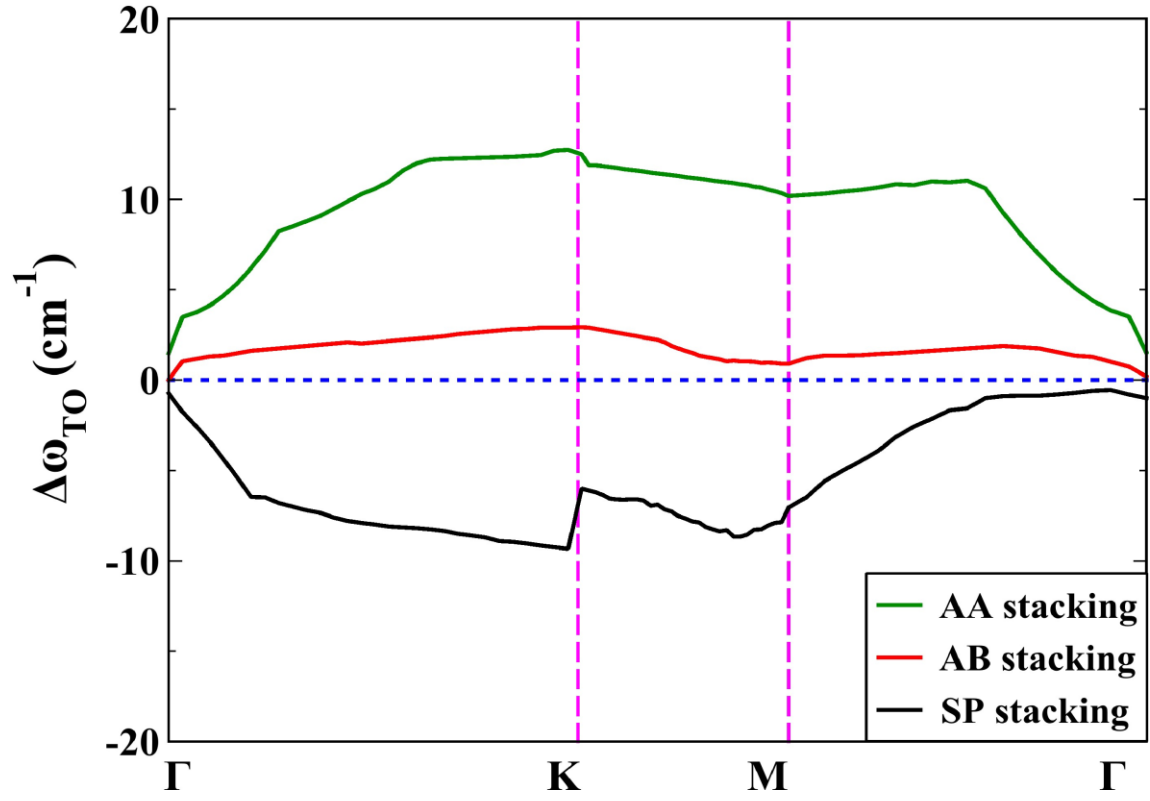


FIG. 8: Transverse optical (TO) phonon frequency difference with respect to TBG system  
 $\theta = 6^\circ$

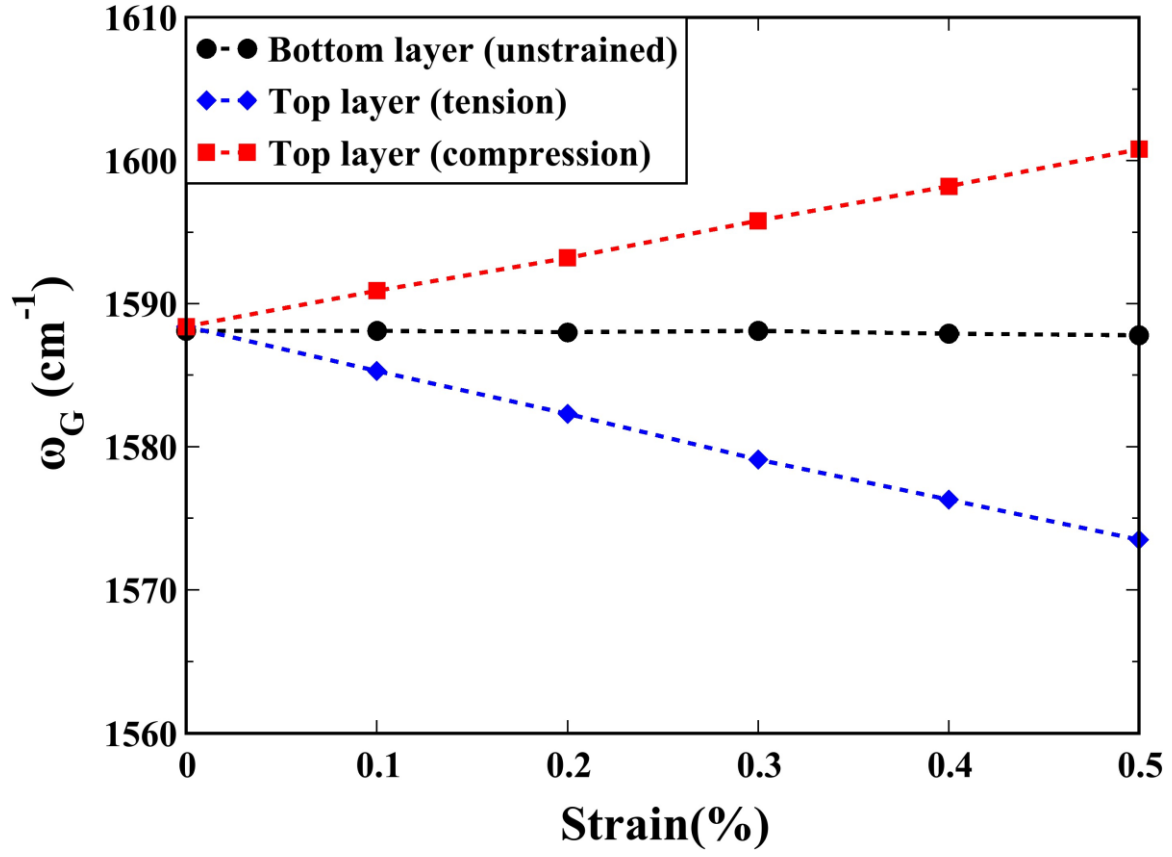


FIG. 9: BOLS predicted Raman G band frequencies of  $\theta = 1.1^\circ$  TBG system as a function of applied heterostrain (tension and compression)

TABLE IV: Calculated  $\beta_{TBG}^\epsilon$  pre-factor values of strained top layer using BOLS parameters with respect to strain

Strain (%)	$\theta = 1.1^\circ$	$\theta = 6^\circ$	$\theta = 13.2^\circ$
0	3.135	3.306	3.466
+0.2	3.207	3.355	3.527
-0.2	3.078	3.214	3.421
+0.5	3.311	3.451	3.619
-0.5	2.988	3.064	3.356
+0.7	3.398	3.506	3.674
-0.7	2.732	2.961	3.312
+1	3.475	3.592	3.773
-1	2.602	2.795	3.248

## REFERENCES

- <sup>1</sup>A. Dey, R. Sharma, S. A. Dar, and H. H. Raza, “A computational investigation on structural, mechanical, electronic, magnetic, thermoelectric, and optical properties of  $\text{CrXpb}$  ( $x = \text{sc, ti}$ ) half-heusler alloys,” *Journal of Superconductivity and Novel Magnetism* **34**, 781–796 (2021).
- <sup>2</sup>A. Dey, B. A. Baraiya, S. Adhikary, and P. K. Jha, “First-principles calculations of the effects of edge functionalization and size on the band gap of  $\text{Be}_3\text{N}_2$  nanoribbons: Implications for nanoelectronic devices,” *ACS Applied Nano Materials* **4**, 493–502 (2020).
- <sup>3</sup>R. Sharma, A. Dey, S. A. Dar, and V. Srivastava, “A dft investigation of  $\text{CsMgX}_3$  ( $x = \text{cl, br}$ ) halide perovskites: Electronic, thermoelectric and optical properties,” *Computational and Theoretical Chemistry* **1204**, 113415 (2021).
- <sup>4</sup>É. D. Murray, K. Lee, and D. C. Langreth, “Investigation of exchange energy density functional accuracy for interacting molecules,” *Journal of Chemical Theory and Computation* **5**, 2754–2762 (2009).
- <sup>5</sup>A. Dey, R. Sharma, S. A. Dar, and I. H. Wani, “Cubic  $\text{PbGeO}_3$  perovskite oxide: A compound with striking electronic, thermoelectric and optical properties, explored using dft studies,” *Computational Condensed Matter* **26**, e00532 (2021).
- <sup>6</sup>A. Dey and D. Chakraborty, “Engineering the band structures of zigzag blue phosphorene and arsenene nanoribbons by incorporating edge corrugations: A first principles exploration,” *Journal of Nanoscience and Nanotechnology* **21**, 5929–5936 (2021).
- <sup>7</sup>V. Kumar, A. Dey, S. Thomas, M. A. Zaeem, and D. R. Roy, “Hydrogen-induced tunable electronic and optical properties of a two-dimensional penta-pt 2 n 4 monolayer,” *Physical Chemistry Chemical Physics* **23**, 10409–10417 (2021).
- <sup>8</sup>J. A. Abraham, R. Sharma, S. Ahmad, and A. Dey, “Dft investigation on the electronic, optical and thermoelectric properties of novel half-heusler compounds  $\text{ScAX}$  ( $x = \text{si, ge, sn, pb}$ ) for energy harvesting technologies,” *The European Physical Journal Plus* **136**, 1091 (2021).
- <sup>9</sup>D. W. Brenner, O. A. Shenderova, J. A. Harrison, S. J. Stuart, B. Ni, and S. B. Sinnott, “A second-generation reactive empirical bond order (rebo) potential energy expression for hydrocarbons,” *Journal of Physics: Condensed Matter* **14**, 783 (2002).
- <sup>10</sup>A. N. Kolmogorov and V. H. Crespi, “Registry-dependent interlayer potential for graphitic

- systems,” *Physical Review B* **71**, 235415 (2005).
- <sup>11</sup>K. Zhang and E. B. Tadmor, “Energy and moiré patterns in 2d bilayers in translation and rotation: A study using an efficient discrete–continuum interlayer potential,” *Extreme Mechanics Letters* **14**, 16–22 (2017).
  - <sup>12</sup>S. A. Chowdhury, K. Inzani, T. Peña, A. Dey, S. M. Wu, S. M. Griffin, and H. Askari, “Mechanical properties and strain transfer behavior of molybdenum ditelluride (mote2) thin films,” *Journal of Engineering Materials and Technology* **144** (2022).
  - <sup>13</sup>X. Gao, H. Sun, D.-H. Kang, C. Wang, Q. J. Wang, and D. Nam, “Heterostrain-enabled dynamically tunable moiré superlattice in twisted bilayer graphene,” *Scientific reports* **11**, 1–8 (2021).
  - <sup>14</sup>C. Androulidakis, E. N. Koukaras, G. Paterakis, G. Trakakis, and C. Galiotis, “Tunable macroscale structural superlubricity in two-layer graphene via strain engineering,” *Nature communications* **11**, 1–11 (2020).
  - <sup>15</sup>A. Stukowski, “Visualization and analysis of atomistic simulation data with ovito—the open visualization tool,” *Model. Simul. Mater. Sci. Eng* **18**, 015012 (2009).
  - <sup>16</sup>W. Zheng and C. Sun, “Energy environ. sci. 4, 627 (2011),”.
  - <sup>17</sup>X. Yang, Y. Wang, J. Li, W. Liao, Y. Liu, and C. Q. Sun, “Graphene phonon softening and splitting by directional straining,” *Applied Physics Letters* **107**, 203105 (2015).
  - <sup>18</sup>J. Campos-Delgado, L. G. Cançado, C. A. Achete, A. Jorio, and J.-P. Raskin, “Raman scattering study of the phonon dispersion in twisted bilayer graphene,” *Nano Research* **6**, 269–274 (2013).
  - <sup>19</sup>Y. Hou, S. Zhang, Q. Li, L. Liu, X. Wu, and Z. Zhang, “Evaluation local strain of twisted bilayer graphene via moiré pattern,” *Optics and Lasers in Engineering* **152**, 106946 (2022).
  - <sup>20</sup>V. Carozo, C. M. Almeida, E. H. Ferreira, L. G. Cancado, C. A. Achete, and A. Jorio, “Raman signature of graphene superlattices,” *Nano letters* **11**, 4527–4534 (2011).
  - <sup>21</sup>F. Gargiulo and O. V. Yazyev, “Structural and electronic transformation in low-angle twisted bilayer graphene,” *2D Materials* **5**, 015019 (2017).
  - <sup>22</sup>A. I. Cocemasov, D. L. Nika, and A. A. Balandin, “Phonons in twisted bilayer graphene,” *Physical Review B* **88**, 035428 (2013).
  - <sup>23</sup>F. Zheng and P. Zhang, “Phonon unfolding: A program for unfolding phonon dispersions of materials,” *Computer Physics Communications* **210**, 139–144 (2017).
  - <sup>24</sup>D. Yoon, Y.-W. Son, and H. Cheong, “Strain-dependent splitting of the double-resonance



raman scattering band in graphene,” Physical review letters **106**, 155502 (2011).

<sup>25</sup>A. Dey, R. Sharma, and S. A. Dar, “An extensive investigation of structural, electronic, thermoelectric and optical properties of bi-based half-huesler alloys by first principles calculations,” Materials Today Communications **25**, 101647 (2020).